INTEGRATED WAVEGUIDE–DETECTOR COUPLER

FOR INTEGRATED OPTICS

AN INTEGRATED WAVEGUIDE–DETECTOR COUPLER FOR INTEGRATED OPTICS

By

Gary Mak, B.Sc.

On–Campus Project

A Project Report
Submitted to the School of Graduate Studies
in Partial Fulfilment of the Requirements
for the Degree
Master of Engineering

McMaster University

June 1988

MASTER OF ENGINEERING (1988)
(Engineering Physics)

McMaster University
Hamilton, Ontario

TITLE: An Integrated Waveguide–Detector Coupler for Integrated Optics

AUTHOR: Gary Mak, B.Sc. (University of Calgary)

SUPERVISOR: Dr. P.E. Jessop

NUMBER OF PAGES: ix, 49

ABSTRACT

The leaky waveguide losses of an integrated waveguide–detector coupler (IWDC) structure in the Corning 7059 glass/SiO_2/silicon system at λ=0.6328 μm has been theoretically modelled and measured as a function of waveguide modal properties, polarization and particularly the SiO_2 cladding layer thickness. Numerous couplers with SiO_2 thicknesses from 0.15 μm to 0.8 μm were measured with coupling values of 400 dB/cm to 1500 dB/cm for TE and to 5800 dB/cm for TM; in good agreement with the four–layer leaky waveguide theory.

We propose and demonstrate the first use of IWDCs as spatially compact optoelectronic crosspoints for switching applications by fabricating and testing a 2x2 switch with silicon photoconductive detectors in the IWDC. The passive power splitting in the integrated switch is close to the ideal fifty percent for a 2x2 matrix but the detectors are not optimum, with evidence of non–ohmic contacts which degrade the crosspoint isolation to best values of 35 dB and an impulse time response of typically 120 ns. For a photogenerated carrier diffusion limited crosstalk from 20 MHz to 340 MHz of –20 dB, crosspoint densities of >160 000 cm^{-2} are possible.

ACKNOWLEDGEMENTS

It is a pleasure to acknowledge Professor P.E. Jessop for his supervision and encouragement during this project and D.M. Bruce for fabricating all the mask sets, expert processing of the devices and general wisdom. Thanks to all the guys in The Sub–Basement for a good time and "the occasional help"!

The author extends appreciation to the Natural Sciences and Engineering Research Council of Canada and McMaster University for their financial support.

TABLE OF CONTENTS

LIST OF ILLUSTRATIONS

Figure

LIST OF TABLES

CHAPTER 1

INTRODUCTION

The field of integrated optics has expanded rapidly since its introduction by S.E. Miller in 1969 [1], who envisioned the integration of microminiature optical devices on a common substrate interconnected by optical waveguides. The hope of integrated optics was to bring about a technological revolution similar to that enjoyed by electronics and integrated circuits (ICs), but for the blossoming optical revolution as optical fibers and lasers emerged. Since then, the thrust of integrated optics has been to develop low–loss waveguides (e.g. [2,51]) and guided–wave devices suitable for integration: optical switches [3], distributed feedback lasers (DFBs) [4], intensity and phase modulators [5–6] and polarizers [7], to name a few. There have been many experiments with co–integrating several devices on a common substrate such as lasers with a back facet monitor detector [8], an 8x8 optical crossbar switch with 64 directional coupler switches [9] and a waveguide integrated with a detector [10].

Integrated optics on silicon substrates has received much of the early attention because of the availability of excellent substrates, state–of–the–art optical detectors below $\lambda=1$ μm and the established electronics technology. Low–loss waveguides have been fabricated for example, with thermally nitrided SiO_2 [11] and sputtered (and laser annealed) Corning 7059 glass [12] with losses as low as 0.06 dB/cm and 0.05 dB/cm, respectively. An integrated waveguide–detector [16], an integrated waveguide p–i–n photodiode array [13], an integrated waveguide/CCD array [14], and a Bragg spectral filter integrated with a waveguide and detector [15] have been demonstrated. Silicon–based integrated optics has suffered in popularity compared to III–V systems because of the lack of monolithically integrated optical sources, although hybrid integration with a GaAs laser is possible.

The motivation of this work has been to fabricate integrated waveguide–detector couplers (IWDCs) as a functional building block and demonstrate applications in an integrated optics context using Corning 7059 glass/silicon as the prototypical waveguide/detector materials. In an IWDC a chosen fraction of the optical power in a waveguide is "tapped" and detected while the remainder continues to propagate in the waveguide. This concept is not new [15], but the control of the coupling has not been demonstrated.

Of course there are functional equivalents to the IWDC. For example, the power in a waveguide can be redirected into another waveguide then terminated with a "conventional" fully absorbing detector using branching Y–junctions or directional couplers, but both require long interaction lengths. For example, to minimize radiation loss the branches in a Y–junction are usually limited to very small angles (<5 degrees) [17], and the directional coupler requires s–bend sections away fom the coupling region which are necessarily long (millimeters) to minimize waveguide curvature losses [18]. As will be shown, the IWDC is spatially compact because the coupling and detection are localized in the same region.

The IWDC has useful applications, for example to distribute point to multi–point electrical signals optically using the IWDC as a partial optical–to–electrical (OE) conversion device, as a monitor detector for a hybridly –integrated diode laser in integrated fiber optic modules and as a switching element in an optoelectronic switching matrix: the latter which we demonstrate in this work.

The description of the power coupling in the IWDCs requires the analysis of the "leaky" waveguide structure in the waveguide/detector coupling region, which depends intimately on the structure. The expected coupling is calculated theoretically and devices were fabricated and tested to confirm the predictions. This work is contained in Chapter 2.

Chapter 3 describes the experiments in demonstrating the potential applications of IWDCs. In particular, we successfully demonstrate the first fully integrated 2X2 optoelectronic switch with two optical inputs and two electronic outputs where the signals are switched by four IWDC crosspoints.

CHAPTER 2

THEORETICAL AND EXPERIMENTAL CHARACTERIZATION OF LEAKY WAVE LOSSES

2.1 Introduction

An integrated waveguide–detector coupler in the Corning 7059 glass/SiO_2/silicon system is illustrated in Fig. 2.1 with the indicated (λ=0.6328 μm) refractive indices and the silicon is strongly absorbing with an absorption coefficient $\approx 3.8 \times 10^3$ cm^{-1} [19–20; see also section 2.5]. The optical photodetector is formed in the silicon substrate, but in this Chapter the emphasis is on the coupling of optical power from the waveguide into the silicon – the propagation loss (of the waveguide). The discussion on the detector fabrication is postponed to Chapter 3.

The IWDC (real) refractive index profile is typical of a well–known class of "leaky" waveguides where optical power in the core can be radiated into the higher index substrate by "optical tunnelling" through the lower index cladding layer. Leaky waveguides are well–known from gas laser [21] and GaAs laser work [23] and some important structures in an integrated optics context has been recently discussed [22].

Far from the IWDC interaction region (point A) the leaky waveguide has low loss for a large SiO_2 layer thickness; a "normal" waveguide (this term is used loosely as there is nothing abnormal about the waveguide in the coupling region). In the IWDC coupling region the SiO_2 layer is tapered to a thickness *d*,

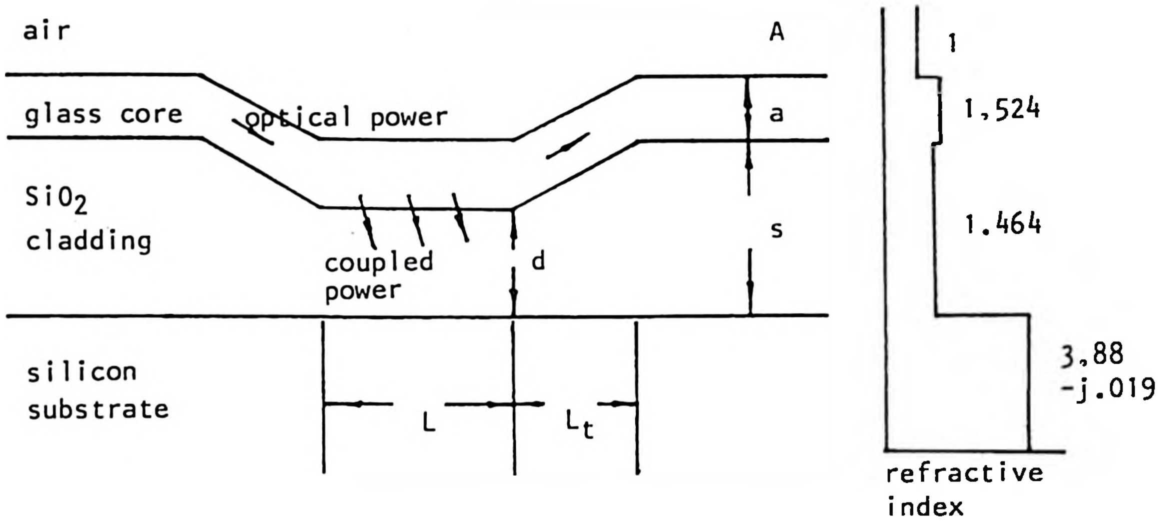

Figure 2.1 Integrated waveguide–detector coupler in the glass/SiO_2/silicon system.

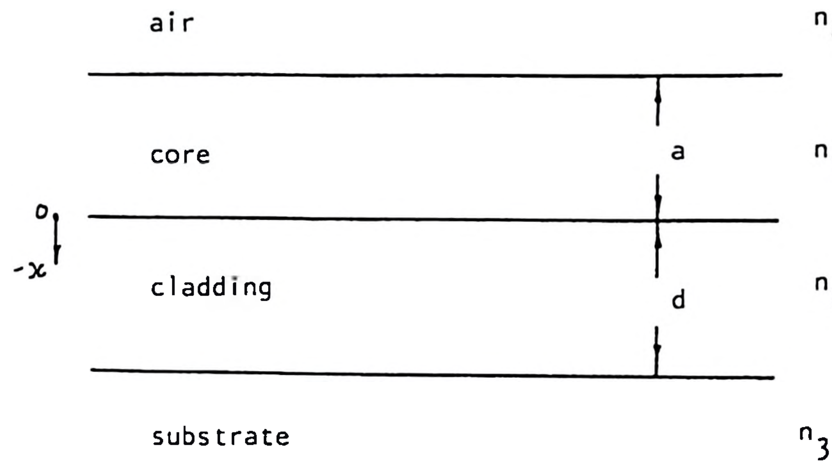

Figure 2.2 Four–layer leaky waveguide.

such that the leaky waveguide loss is high. The total loss should be dependent on d and the length L, or simply if the leaky waveguide has a loss coefficient (units ≡ inverse distance) then it is simple to calculate the total loss given L. In the rest of this work, loss shall mean the loss coefficient and will be distinguished from the total loss.

The goal of this Chapter is to calculate the loss given the waveguide structure and refractive indices; particularly the dependence of loss on d.

2.2 Theory of Leaky Waveguides

The leaky wave loss of the structure shown in Fig. 2.1 can be analyzed by exact numerical solution of Maxwell's equations, by an approximate perturbation solution [23] or by an analytic theory of three–layer leaky structures (i.e. $d = 0$) [24] and extended to the four–layer case. The exact numerical solution by the zero element method [25] and its application to a wide variety of integrated optical slab waveguides, particularly leaky ones, has been discussed at length elsewhere [22]; only the results will be presented.

Solution by the zero element method (implemented in the computer code NWG_56 [22]) was convenient because it was an existing general n–layer slab waveguide analysis tool, but direct numerical solution of the four–layer waveguide eigenvalue equation is equivalent and straightforward and has been done in the literature [11]. In addition, to verify that the zero element solutions were correct the calculated results were substituted into the eigenvalue equation.

The four–layer waveguide shown in Fig. 2.2 has the eigenvalue equation which determines the allowed modes [26]

$$
\begin{aligned}
ah_1 = \quad & N\pi + \tan^{-1}\{\eta_{14}h_4/h_1\} \\
& + \tan^{-1}\{\eta_{12}h''_2 \tanh[j\tan^{-1}\{\eta_{23}h''_3/h''_2\} + dh''_2]\}
\end{aligned} \tag{1}
$$

with

$$
\begin{aligned}
& h_1^2 = k_o^2 n_1^2 - \beta^2 \\
& h_2''^2 = \beta^2 - k_o^2 n_2^2 \\
& h_3''^2 = k_o^2 n_3^2 - \beta^2 \\
& h_4^{\,2} = \beta^2 - k_o^2 n_4^2 \\
& \eta_{ij} \qquad = n_i^2/n_j^2 \qquad \text{TM modes} \\
& \qquad\quad\;\; = 1 \qquad\qquad \text{TE modes}
\end{aligned} \tag{2}
$$

where N=0,1,2,... is the mode order, β is the propagation constant (such that the electric and magnetic field varies as $e^{j\beta z}$ where z is the propagation direction), $k_o=2\pi/\lambda_o$, λ_o is the free space wavelength, $j=\sqrt{-1}$ and a and d are the waveguide thickness and cladding layer thickness, respectively.

The modal and loss characteristics are obtained by solving equations (1) and (2) for the real and imaginary part of β (say β_r and β_i) in the range $n_4k_o < \beta \leq n_1k_o$ which are the substrate leaky modes. There are additional leaky modes for $\beta < n_4k_o$, but they are air and substrate leaky modes which are undesirable since power radiating into the air is lost, whereas radiation into the substrate is absorbed by the silicon. The power loss coefficient for a mode is given by $-2\beta_i$.

The approximate perturbation analysis (for TE modes) treats the four–layer leaky waveguide of Fig. 2.2 as a perturbation of the (non–leaky) three–layer waveguide ($d\to\infty$), i.e. the propagation constant for the four–layer waveguide is given as $\beta=\beta_o+\delta\beta$, where β_o is the propagation constant of the three–layer waveguide and $\delta\beta$ is the perturbation. The result to first–order is [23]

$$\delta\beta = (2U_o/\beta_o)\exp(-2p_o d)[(p_o-\gamma+jr)/(p_o+\gamma-jr)] \times \{U_o(p_o^{-2}+h_o^{-2})(1+p_o a)+q_o(q_o^{-2}+h_o^{-2}) \times [\cos(h_o a)/p_o+\sin(h_o a)/h_o]\}^{-1} \quad (3)$$

with

$$U_o = \cos(h_o a)+(q_o/h_o)\sin(h_o a) \quad (4)$$

$$r+j\gamma = [n_3^2k_o^2-\beta_o^2-\alpha_s^2/4+j\alpha_s n_3 k_o]^{1/2} \quad (5)$$

where α_s is the bulk absorption coefficient of the substrate, (i.e. the substrate complex index is $n_3-j\alpha_s/2k_o$), the power loss coefficient is given by

$$\alpha = 2\,\mathrm{Im}\,(\delta\beta) \quad (6)$$

and β_o, q_o etc. are determined from the well–known three–layer asymmetric slab waveguide eigenvalue equation [26]

$$\tan(ah_o)=h_o(p_o+q_o)/(h_o^2-p_oq_o) \quad (7)$$

where
$$h_o^2 = n_1^2k_o^2-\beta_o^2$$
$$p_o^2 = \beta^2-n_2^2k_o^2$$
$$q_o^2 = \beta^2-n_4^2k_o^2 \quad (8)$$

and for guided modes $n_2k_o \leq \beta \leq n_1k_o$. Solution of equation (7) and (8) with the results plotted as normalized design curves have been published [27].

The salient result (equation (3)) is the inverse exponential dependence of loss on the cladding layer thickness d and the inverse penetration of the optical field into the cladding layer p_o; the latter is more obvious if the electric field of the mode in the cladding is written as $E \propto e^{-(p_o x)}$.

The approximate analytic result for the loss of the three–layer leaky waveguide (d=0, $p_o^2=\beta^2-n_s^2k_o^2$; and different from the the three–layer non–leaky waveguide described by equations (7) and (8)) is [24]

$$\alpha_{TE} \approx (2\pi^2(N+1)^2/k_o^2n_1^2)\ a^{-3}((n_2/n_1)^2-1)^{-1/2} \tag{9}$$

for TE modes, and using the approximate result (equation (3)) that the loss is proportional to $e^{-(2p_od)}$, the result is extended to the four–layer case and the loss is given by

$$\alpha'_{TE} \approx \alpha_{TM}\, e^{-2k_od\sqrt{(n_1^2-n_2^2)}} \tag{10}$$

and for TM modes,

$$\alpha_{TM} \approx \alpha_{TE}(n_2/n_1)^2 \tag{11}$$

2.3 Numerical Investigations of Leaky Structures

In this section the leaky propagation loss versus waveguide core (glass) thickness, cladding layer (SiO_2) thickness and polarization as well as the modal properties will be examined. The approximate results are compared to the exact numerical method to set bounds on their validity.

Plotted in Fig. 2.3 is the leaky loss (of the structure depicted in Fig. 2.1) with d=0 for all TE modes. Plotted in Fig. 2.4 is the loss versus SiO_2 thickness d for a=0.6 μm and 0.7 μm for the TE_0 and TM_0 modes: calculations for both these figures are exact. There are a number of interesting results. As expected, the four–layer waveguide has more flexibility for tailoring the loss than with only three layers because the cladding layer thickness is independent of the waveguide core thickness. It is particularly interesting that the four–layer waveguide can achieve lower loss than the three–layer one while "single–mode" (for the "normal"

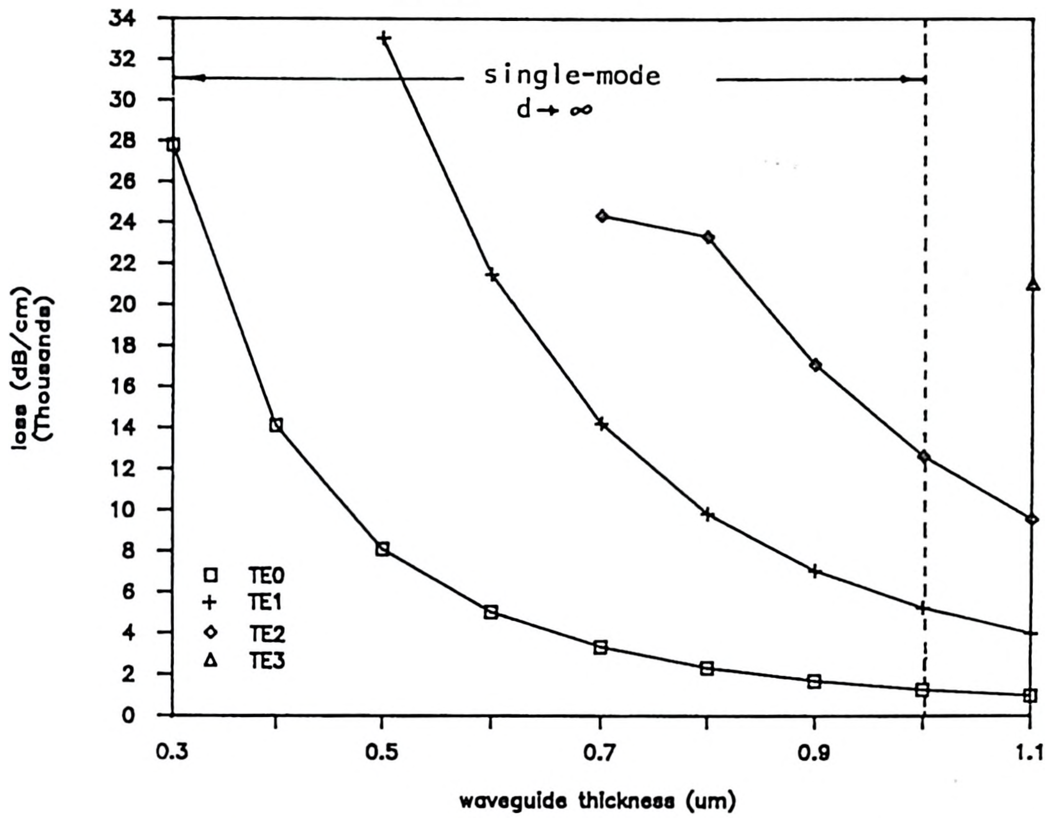

Figure 2.3 TE_0, TE_1, TE_2 and TE_3 leaky wave loss for d=0.

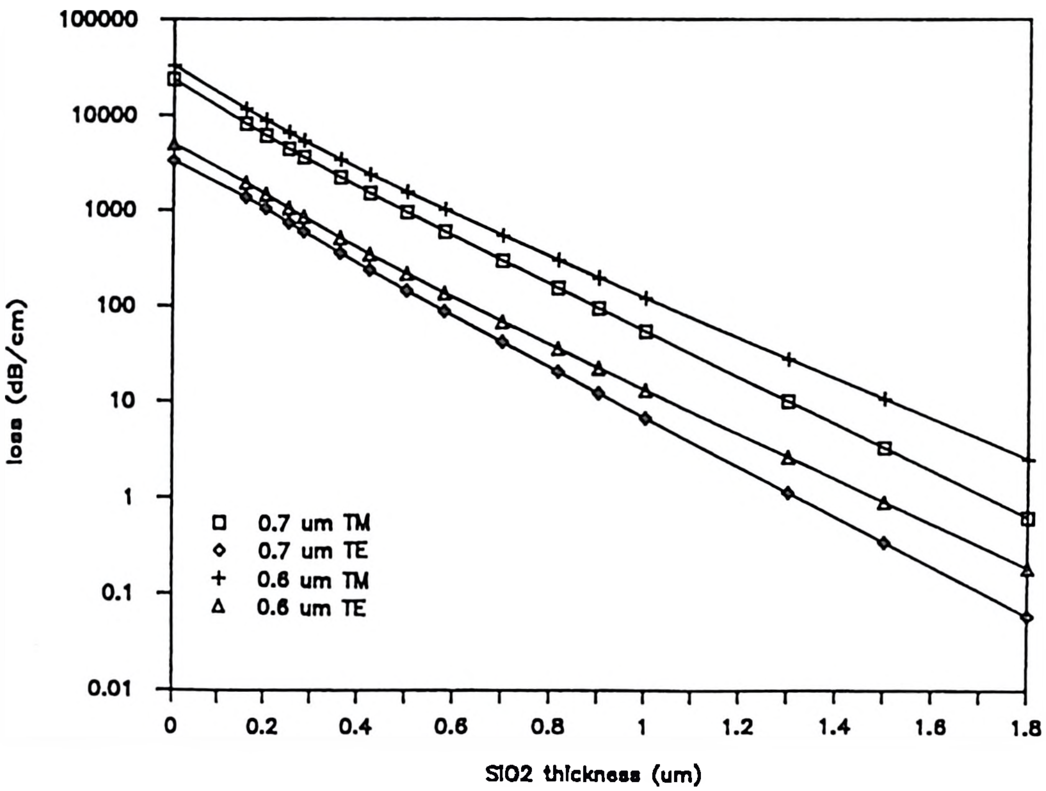

Figure 2.4 TE_0 and TM_0 leaky loss for the structure of Fig. 2.2 versus SiO_2 thickness (d).

waveguide in the limit $d \to \infty$, i.e. 0.3 μm$\lesssim a \lesssim$1.0 μm; also see below) which has a minimum loss of $\approx$1500 dB/cm. This is important for low coupler value IWDCs where maximum control of the coupling is required. Also for a=0.6 μm for example, compare the maximum TE_0 and TM_0 loss of $\approx$ 5000 dB/cm and 32700 dB/cm compared to the bulk absorption of 16500 dB/cm, i.e. the leaky losses can be higher than the bulk substrate absorption (more later).

The IWDC should be single–mode because the loss increases strongly with mode order (see Fig. 2.3 and equation (9)) and in a hypothetical multi–mode IWDC, mode conversion and variable mode launching conditions at the waveguide input can cause randomness in the coupler loss. For our leaky waveguides this ideal single–mode state is difficult to achieve because tailoring the leaky losses by varying a or d also changes the mode structure. The former case is illustrated in Fig. 2.3. The single–mode regime for d=0 is 0.3 μm$\lesssim a \lesssim$0.5 μm whereas the non–leaky ($d \to \infty$) single–mode regime is 0.3 μm$\lesssim a \lesssim$1.0 μm. Thus the leaky waveguide restricts the waveguide thickness to smaller values, which can be a problem since for the "normal waveguide" in this restricted waveguide thickness range, for s=1.8 μm (see section 2.5) the leaky losses are $\gtrsim$0.9 dB/cm for TE and $\gtrsim$5 dB/cm for TM; not a "low–loss" waveguide. Of course this problem could be rectified by increasing s, but practically this is difficult because the thermal growth of SiO_2 increases logarithmically with time. The situation is worst for four–layer leaky waveguides (with a finite value of d). As d increases, the effective leaky mode waveguide thickness increases and more leaky modes can propagate compared to the three–layer leaky structure. Simultaneously, the single–mode regime decreases and for large d there is a point where for even a=0 the waveguide is multi–mode – the SiO_2 becomes the waveguide core.

In summary, this discussion lead to two important points: (1) in the coupling region it is difficult to make the leaky waveguide single–mode while keeping the "normal" waveguide low loss, and (2) for the low–loss waveguide a large SiO_2 thickness results in many leaky modes, for example there are nine leaky TE modes for a=0.7 μm and s=1.8 μm. Practically, a true single–mode system is difficult to obtain.

The problem of multi–mode propagation should not be too severe if the "normal" waveguide is designed for "single–mode" operation (defined for $d \to \infty$), since for large enough s the lowest order leaky mode is akin to the true guided mode whose mode confinement is determined by the glass/SiO_2 interface, whereas all higher leaky modes will be determined by the SiO_2/silicon interface, i.e. the mode is not primarily guided in the glass. These latter modes are high loss and as observed experimentally with short (1–1.5 mm) waveguide samples these higher order modes are attenuated rapidly: we can view the mode launching as single–mode. The consideration of possible mode conversion in the coupling region or tapers will be digressed to the paragraphs following the taper design discussion (in section 2.4).

There are other important observations. There is a strong anisotropic polarization–dependent loss in the structures because of the large ratio of the substrate index to the waveguide core index, i.e. $\alpha_{TM}/\alpha_{TE} \approx (n_3/n_1)^2 \approx 6.5$ (equation (11)). This has important ramifications for practical applications, since the device will not be polarization independent and as discussed in section 2.6 nonidealities such as waveguide depolarization (polarized mode conversion) may change the expected loss.

If the absorption in the substrate is ignored (i.e. assume the complex refractive index of silicon is $3.88-j0$), the results of Fig. 2.4 are changed little. This can be seen from equations (3) to (6), where if equation (5) is written

$$r \approx [\alpha^2+\sigma^2]^{1/4}$$

$$\gamma \approx r\,\sigma/2\alpha \qquad \text{for } \sigma<<\alpha \tag{12}$$

and

$$\alpha = n_S^2k_O^2-\beta_O^2-\alpha_S^2/4$$

$$\sigma = \alpha_S n_S k_O \tag{13}$$

Numerically $\alpha = k_O^2(3.88^2-(\beta_O/k_O)^2-0.019^2)$ and $\sigma = k_O^2(0.148)$ with loss in the substrate and $\alpha = k_O^2(3.88^2-(\beta_O/k_O)^2)$ and $\sigma = 0$ without loss. The range of β is $n_4< \beta/k_O <n_1$ so r changes little with loss and has a maximum value of $3.57k_O$ and γ is directly dependent on the loss with a maximum value of $0.039k_O$. Inspection of equation (3) shows that the absorption coefficient of the substrate has negligible effect on the propagation loss if $p_O>>\gamma$ (see the following discussion concerning p_O and the validity of the perturbation results). For example for a=0.6 μm, $p_O \approx 0.27k_O >> .039k_O$ thus, the proper physical interpretation is that the guided–wave optical power "leaks" out of the waveguide and is then absorbed in the characteristic length given by the bulk absorption coefficient. This physical description is important; the loss is determined by the geometry of the structure and not the bulk absorption coefficient. This is not detrimental, but the proper physical interpretation helps to design more useful structures. For example, consider the ray optic picture shown in Fig. 2.5 of a waveguide integrated with a vertical p–i–n detector. The effective absorption length of the detector is smaller than for the bulk case with a possible reduction in the carrier transit time. For a long enough

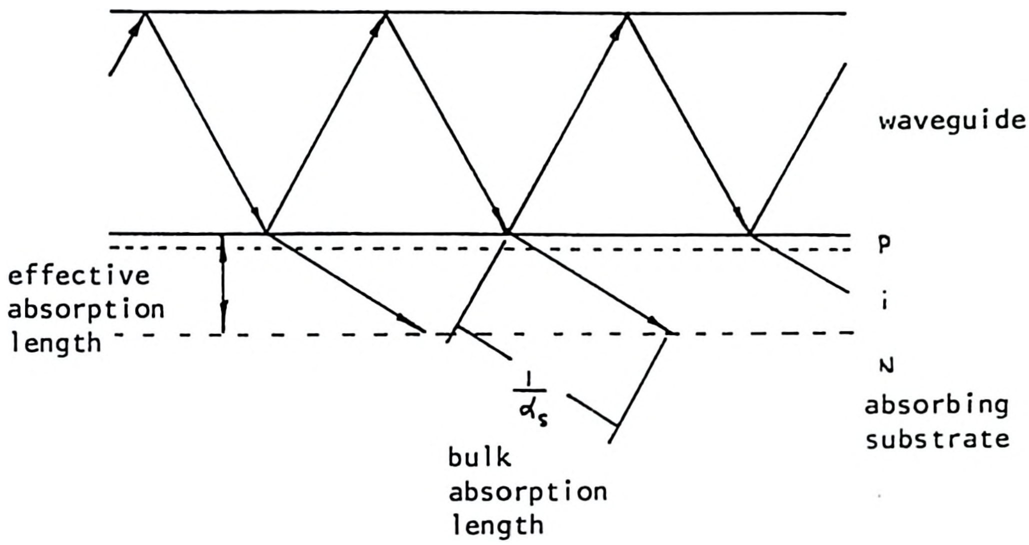

Figure 2.5 Waveguide integrated with a p–i–n detector.

waveguide (absorption length) there is a gain in speed for no loss in quantum efficiency [34].

The above arguments do not apply to all leaky structures in general. In fact the absorption coefficient of the substrate is important when $n_1 \approx n_2 \approx n_3$ or approaching (non–leaky) waveguide cut–off as $p_0 \approx \gamma$: the latter is understandable since near cut–off most of the optical power is not confined in the core but in the cladding. Also the statement that the loss is independent of the bulk substrate absorption is not true since by the usual Kramers–Kronig relations the absorption is inextricably related to the real index which is important in determining the leaky wave losses.

Plotted in Fig. 2.6(a)–(d) is the TE_0 mode loss versus cladding layer thickness for four waveguides of $V=k_0 a\sqrt{(n_1^2-n_2^2)}$ of 2.04 (n_1=1.522,n_2=1.483,a=0.6 um), 2.38 (n_1=1.522,n_2=1.483,a=0.7 um), 2.94 (n_1=1.52,n_2=1.46,a=0.7 um) and 3.78 (n_1=1.52,n_2=1.46,a=0.9 um). The approximate range of single–mode operation is $1.2 \lesssim V \lesssim 4.2$ [27]. The loss is calculated by three methods: the exact numerical zero element method, the approximate perturbation method and the approximate analytic solution.

The TM_0 mode loss for the same V numbers is plotted in Fig. 2.7(a)–(d). The approximate perturbation and analytic methods are taken from the TE results and multiplied by $(n_3/n_1)^2$ (as discussed above), whereas the zero element method is exact for TM modes.

As seen in Figs. 2.6(a)–(d), the perturbation results for TE modes are in excellent agreement with the exact computer results for large V numbers with slight differences at the highest loss. The difference at low V number, for example

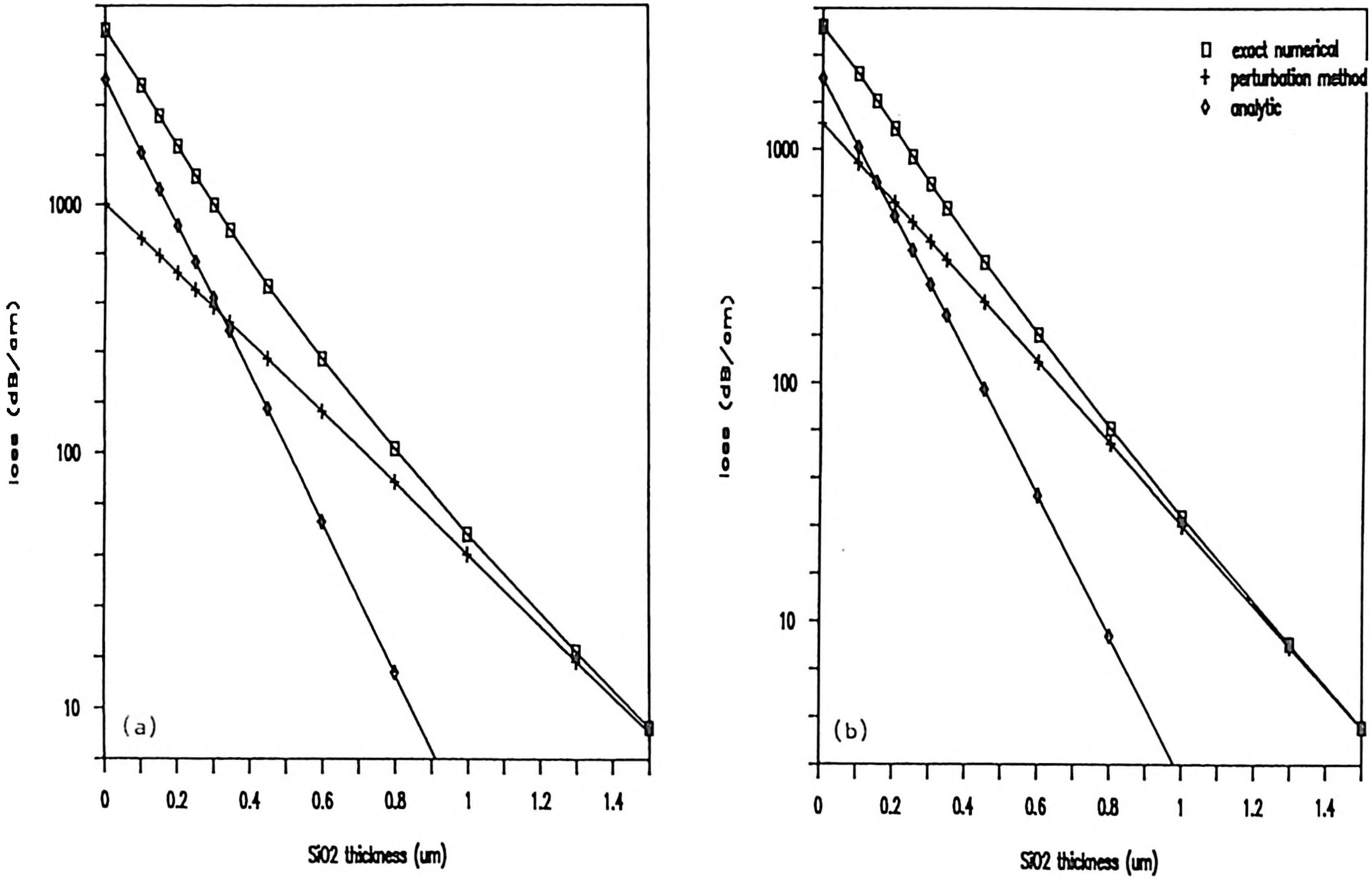

Figure 2.6 TE_0 loss versus the SiO_2 thickness for four different waveguides calculated by three methods, V=2.04 (a) and V=2.38 (b).

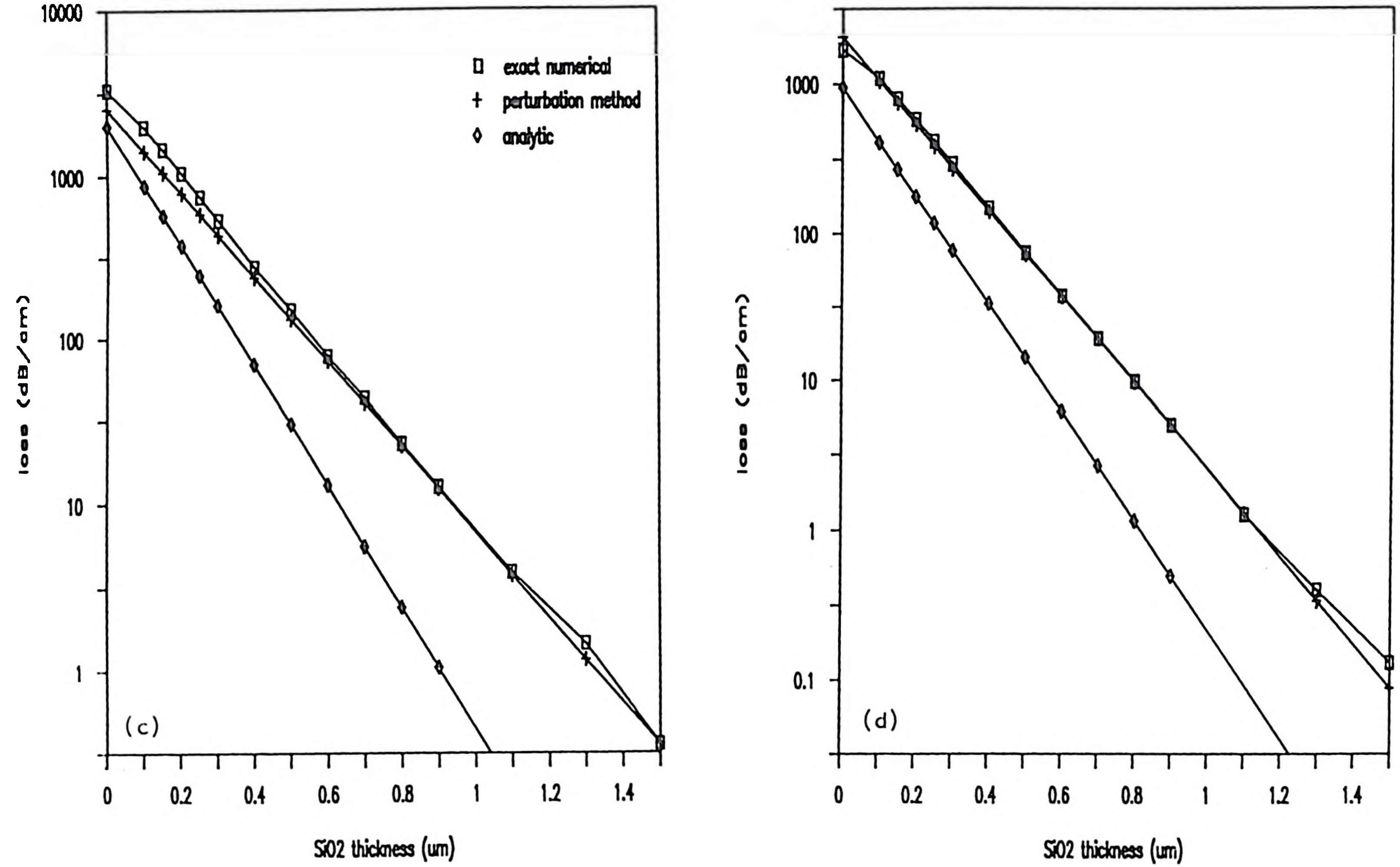

Figure 2.6 TE_0 loss versus the SiO_2 thickness for four different waveguides calculated by three methods, V=2.94 (c) and V=3.78 (d).

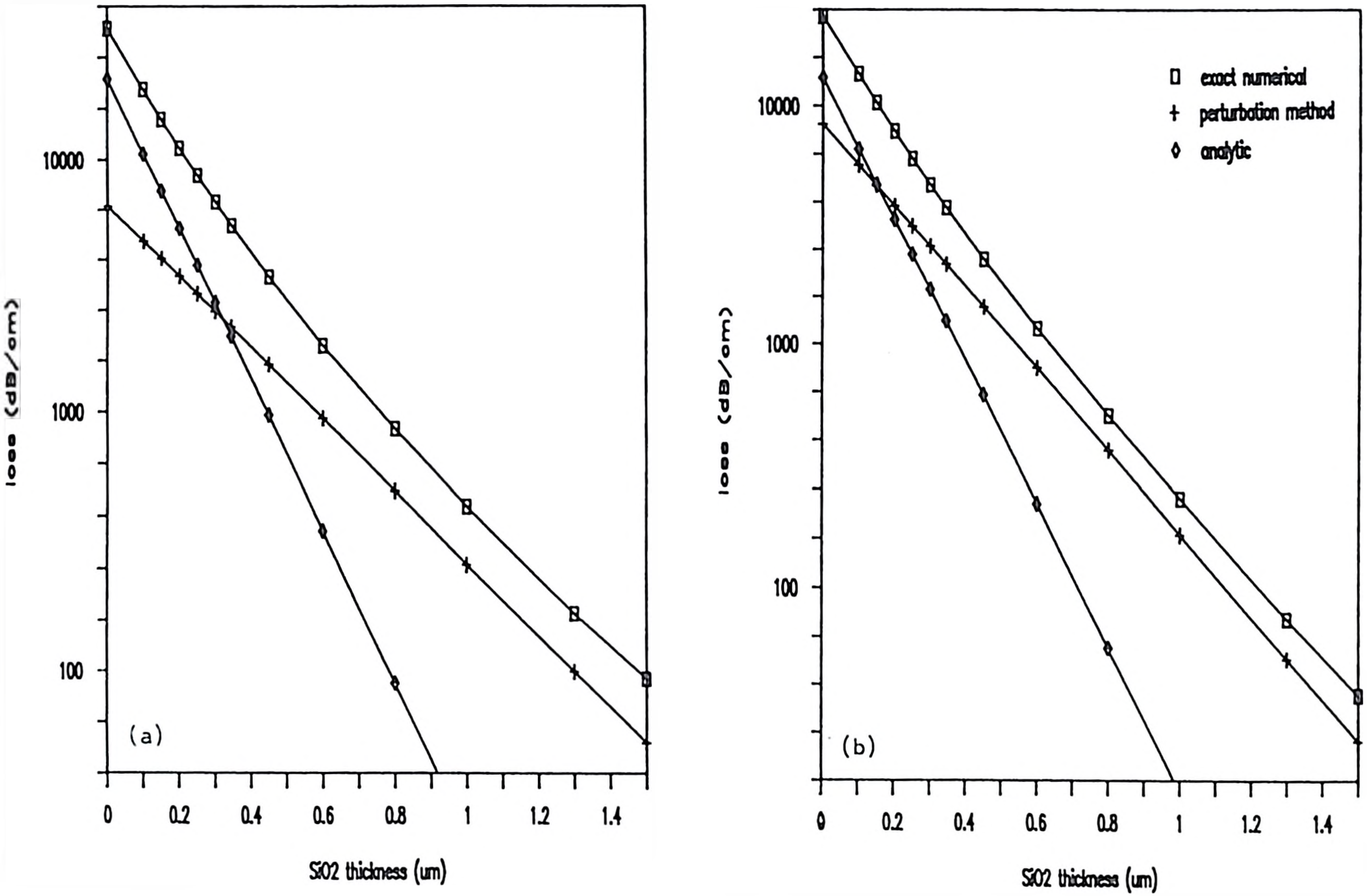

Figure 2.7 TM_0 loss versus the SiO_2 thickness for four different waveguides calculated by three methods, V=2.04 (a) and V=2.38 (b).

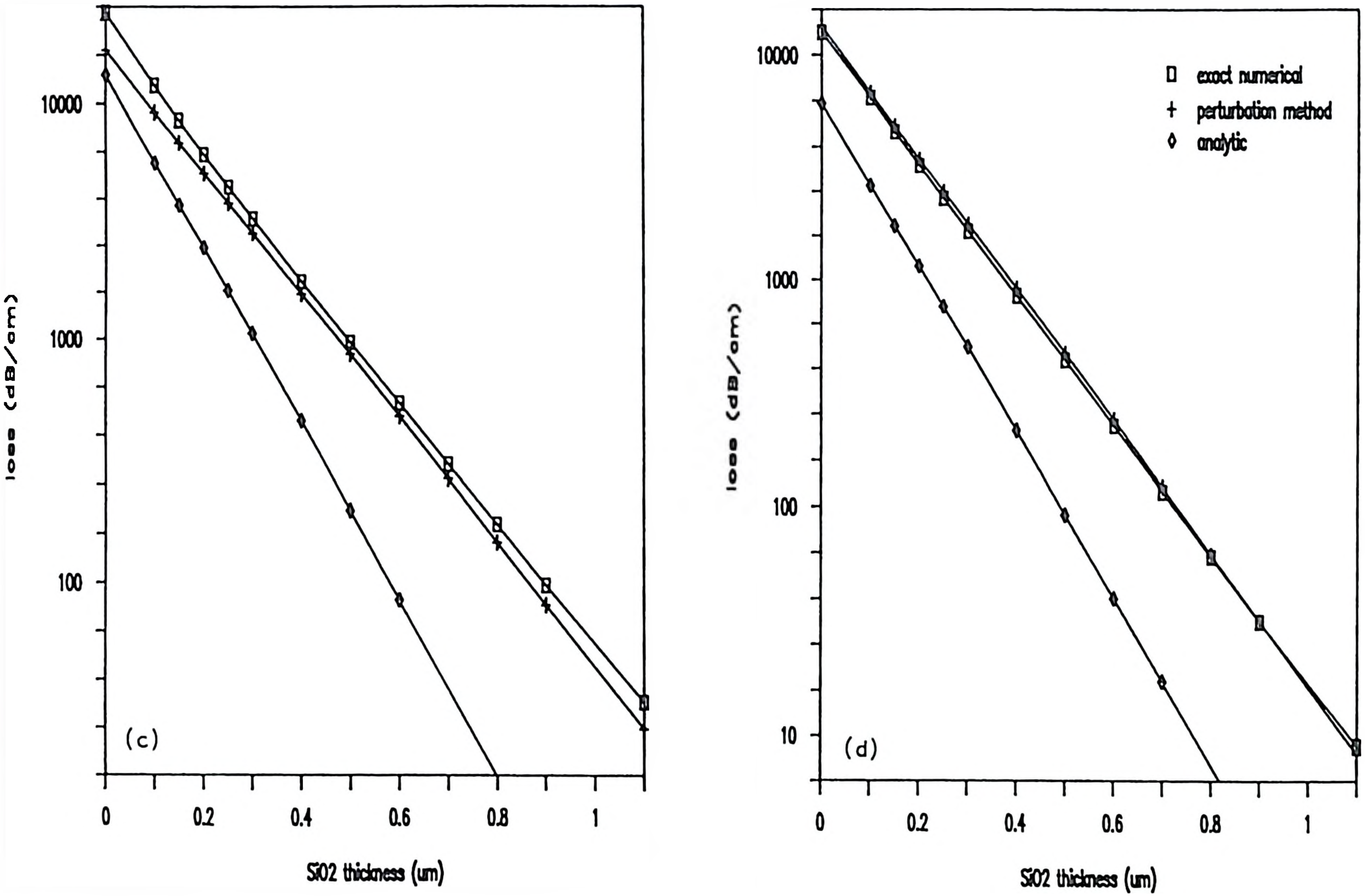

Figure 2.7 TM_0 loss versus the SiO_2 thickness for four different waveguides calculated by three methods, V=2.94 (c) and V=3.78 (d).

for the case V=2.04, is significant even when the losses are "as low as" 30 dB/cm. The divergence of the approximate theory from the exact results is due to the strong perturbation of the real propagation constant β_r with decreasing d. Consider the transverse wavevector h''_2, which as seen in equation (3) strongly affects the loss (i.e. exponentially dependent on $p_o \approx h''_2$ in the small perturbation regime, $\beta \to \beta_o$). Rewriting h''_2 with $\beta = \beta_o + \delta\beta_r + j\delta\beta_i$ where $\delta\beta_r = \mathrm{Re}(\delta\beta)$ and $\delta\beta_i = \mathrm{Im}(\delta\beta)$,

$$h''^2_2 = p_o^2 + [2\beta_o\delta\beta_r + (\delta\beta_r)^2 - (\delta\beta_i)^2] + j2\delta\beta_i(\beta_o + \delta\beta_r) \tag{14}$$

For the three–layer (non–leaky) waveguide $p_o \to 0$ as $\beta_o \to k_o n_2$ or as the waveguide approaches cut–off (small V number) and because of the second term on the RHS of equation (14), h''_2 (for the four–layer (leaky) waveguide) can be very different from p_o. This difference invalidates the perturbation method because the original assumption that the four–layer waveguide is a slightly perturbed three–layer waveguide is violated. Thus the criterion for the validity of the perturbation theory is

$$p_o^2 >> [2\beta_o\delta\beta_r + (\delta\beta_r)^2 - (\delta\beta_i)^2] \tag{15}$$

Plotted in Fig. 2.8(a)–(b) is $\delta\beta_r/k_o$ and $\delta\beta_i/k_o$, respectively, calculated by the zero element method for the example of V=2.04 and where $\beta_o = 1.492k_o$ and $p_o = 0.162k_o$ for TE. From equation (15), the perturbation results are valid for $\delta\beta_r/k_o << 0.0088$, which is not easy to satisfy as even at $d = 0.8$ μm $\delta\beta_r/k_o \approx 0.002$.

Although $\delta\beta_r$ and $\delta\beta_i$ were calculated exactly for the example of Fig. 2.8, obviously the perturbation result for $\delta\beta$ (equation (3)) is normally used as a

12a

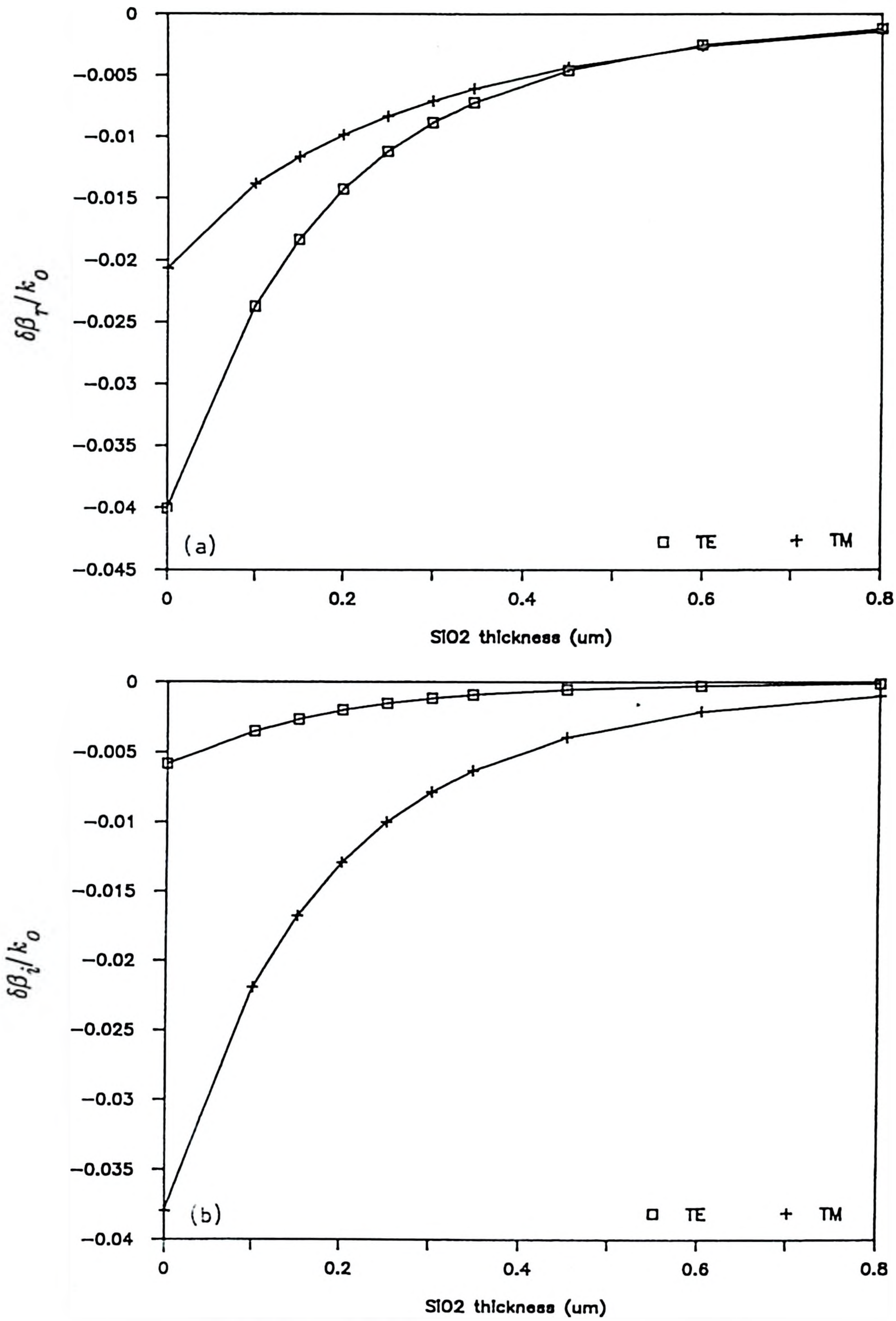

Figure 2.8 $\delta\beta_r/k_o$ and $\delta\beta_i/k_o$ versus SiO_2 thickness for the leaky waveguide a=0.6 μm.

self–consistent validation of the perturbation method along with equation (15).

The TM approximate results using the handy rule $\alpha_{TM}/\alpha_{TE} \approx (n_3/n_1)^2$ are in good agreement with the exact answers for larger V number. Thus for well confined waveguides the design of IWDCs with the approximate perturbation analysis is adequate to fully understand the loss and polarization properties without extensive and time–consuming analysis by exact numerical methods, even though for this work the exact results have been used throughout.

The analytic results provide useful estimates of the loss and are surprisingly good (within a factor of 2) for larger V number and small *d*.

As shown in Fig. 2.4 the "normal" waveguide with s=1.8 μm (see section 2.6) will be low loss for TE modes and will have a small but non–negligible loss for TM modes (few dB/cm).

2.4 Design of Tapers for IWDCs

Section 2.3 has discussed the dependence of loss on the leaky waveguide structure in the coupling region of length L (Fig. 2.1). This section is concerned with the details of tapering the SiO_2 thickness from the low loss "normal" waveguide (A of Fig. 2.1) to the coupling region, namely the minimum taper length L_t (Fig. 2.1) required such that extraneous and non–reproducible losses are negligible. These non–leaky losses are undesirable for two reasons: they confuse the accurate measurement of the leaky losses and they can be strongly dependent on the taper length which forces the fabrication to be critical. The two loss mechanisms that place a lower limit on the taper length is the loss due to radiation in a curved waveguide section and in abrupt tilts. The relative significance of the two is illustrated by assuming a taper with a fixed radius of curvature (Fig. 2.9(a)) and an abruptly tilted linear taper (Fig. 2.9(b)). For these calculations a non–leaky waveguide ($d \to \infty$) is assumed; the discussion of this assumption will be postponed (see below).

Physically, the loss of power in a curved waveguide originates from the field far from the waveguide which cannot follow the core power through the bend since the field would need to propagate faster than the velocity allowed in the outside medium [28]. The radius of curvature losses for the symmetric three–layer waveguide [28–29] and the weakly–guiding asymmetric waveguide (with small asymmetry) [30] has been recently studied; but, our waveguides are strongly asymmetric. We simply extend the theory of Marcuse [29] for the symmetric case to the asymmetric case (Fig. 2.10) with the result that the power loss coefficient versus the radius of curvature R is

$$\alpha_R = 2h_o^2 q_o \, e^{(-\beta_o \tanh^{-1} q_o/\beta_o + q_o)2R} \, e^{(q_o a)} \times \\ [|\beta_o|(a+1/q_o+1/p_o)(h_o^2+q_o^2)]^{-1} \qquad (16)$$

It is not surprising that the loss depends strongly on q_o (equation 16) which is a measure of the field extent on the "outside curve", i.e. $E(x) \propto e^{-(q_o(x-a/2))}$ for $x \geq a/2$. This formula is valid within a factor of $e^{(q_o a)}$ which follows from the definition of the radius of curvature; we define it as the center of the waveguide (Fig. 2.10) but anywhere within the waveguide is physically correct. The above equation is valid when the evanescent field (with transverse wavevector q_o) on the outside of the bend is very similar to the unbent slab waveguide. For high loss this is not the case as the peak field in the waveguide moves toward the outer edge into

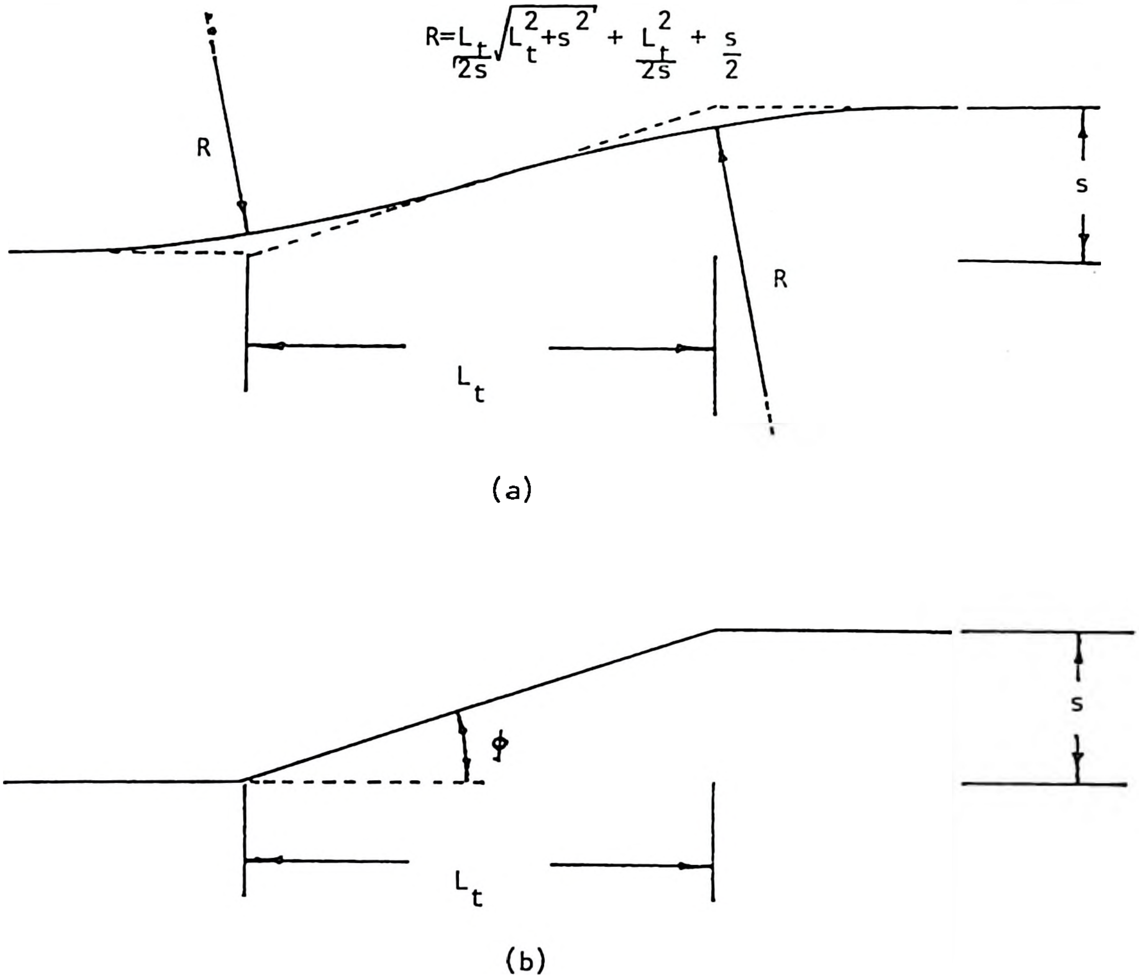

Figure 2.9 Two ideal taper shapes: single radius of curvature taper (a) and a linear tilted taper (b).

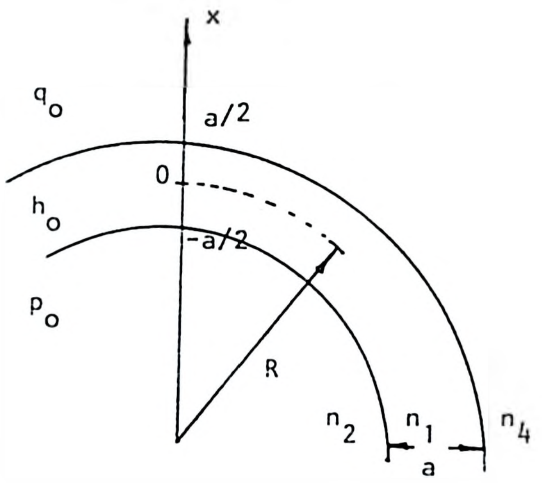

Figure 2.10 Curved asymmetric slab waveguide of radius R.

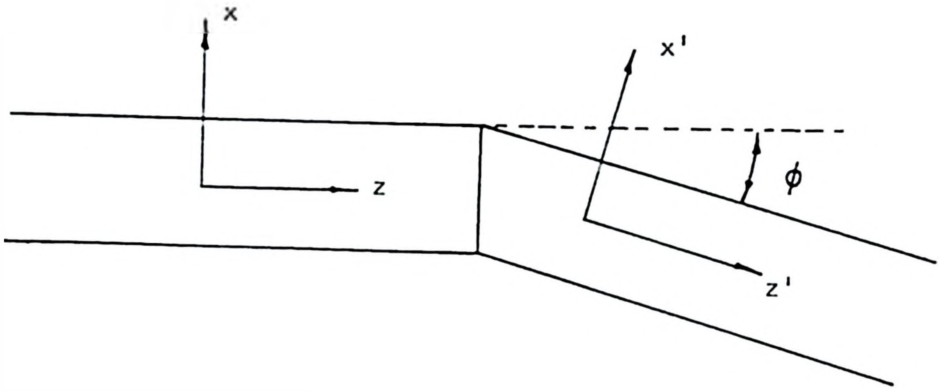

Figure 2.11 Tilted waveguide.

the edge–guidance mode regime [30]. An approximate validity criteria for equation (16) can be derived.

Consider the wave equation for the electric field in a curved waveguide coordinate system [30],

$$d^2E/dx^2+[k_o^2\, n^2(x)-(\beta^2-1/(4R^2))/(1+x/R)^2]E=0 \tag{17}$$

where $n(x)$ is the waveguide index profile and as expected, for $R\to\infty$ the term in the square brackets approaches $k_o^2 n(x)^2-\beta^2$ which is the usual straight waveguide result. We set the validity constraint as

$$(\beta^2-1/(4R^2))/(1+x/R)^2-\beta^2 << (n_1^2-n_2^2)k_o^2$$

i.e. the change in propagation constant is small compared to the allowed propagation values $k_o n_1 \lesssim \beta \lesssim {}_o n_2$, or

$$R >> x/(n_1-n_2)$$

The approximate maximum value of x should be chosen such that the field is small and since the field radiates from the outside curved region, let $x=x_{max}\approx 3/q_o$ so

$$R >> 3/q_o(n_1-n_2) \tag{18}$$

is the required criteria.

At the junction of a tilted waveguide (Fig. 2.11), the mismatch in the waveguide field profiles cause radiation and reflection losses. The coupling efficiency η of the mode in waveguide section 1 to section 2 is given by [31]

$$\eta = |\int E(x)E(x/\cos\phi)^* e^{j\beta x\tan\phi}\, dx|^2 \tag{19}$$

where $E(x)$ is the power normalized waveguide mode electric field profile, for small tilt angles ϕ, $E_1(x)\approx E_2(x)\approx E(x)$ and the integration is over the infinite waveguide cross–section. An approximate expression for η has been given by Marcuse [32] for symmetric waveguides, but is reasonably valid for an arbitrary waveguide where the mode profile is Gaussian–like:

$$\eta \approx \exp[-(\omega_0 n_1 k_0 \phi/4)^2] \tag{20}$$

where ω_0 is the $1/e^2$ full mode power width and for weakly–guiding waveguides $n_1 \approx n_2$. The approximate expression readily demonstrates the strong dependence of coupling efficiency on tilt angle. For example if ω_0=1 μm, a tilt angle of 3.3 degrees has a loss of 0.2 dB.

Plotted in Fig. 2.12 is the two taper loss (in dB) for the curved taper and the tilted taper (exact and approximate) versus taper length L_t for a=0.70 μm, s=1.8 μm and ω_0=0.9 μm. The curvature losses are negligible for taper lengths $\geq$ 15 μm while the tilt losses are still $\approx$ 0.2 dB for taper lengths exceeding 50 μm, thus smooth transition tapers are desirable. The validity of the curvature loss results in Fig. 2.12 are (equation (18)) $R >> 5$ μm and $R >> 17$ μm or $L_t >> 3$ μm and $L_t >> 6$ μm for the air/glass interface and glass/SiO_2 interface on the "outside" of the curve, respectively. The results in Fig. 2.12 are for TE modes, but are similar for TM modes because of the near TE–TM degeneracy (see section 2.6).

The radiation mechanisms discussed above do not necessarily degrade the waveguide–detector coupling efficiency, i.e. the efficiency of light lost out of the waveguide <u>and</u> subsequently absorbed in the silicon. For example, the curvature losses are predominantly from the curved taper near the coupling region (in Fig. 2.9(a)) because of the large field extent into the cladding layer as $n_1 - n_2 \approx .06$: this radiation into the substrate (silicon) does not reduce the coupling efficiency. In contrast the field penetration into the air is small because of the large air/glass

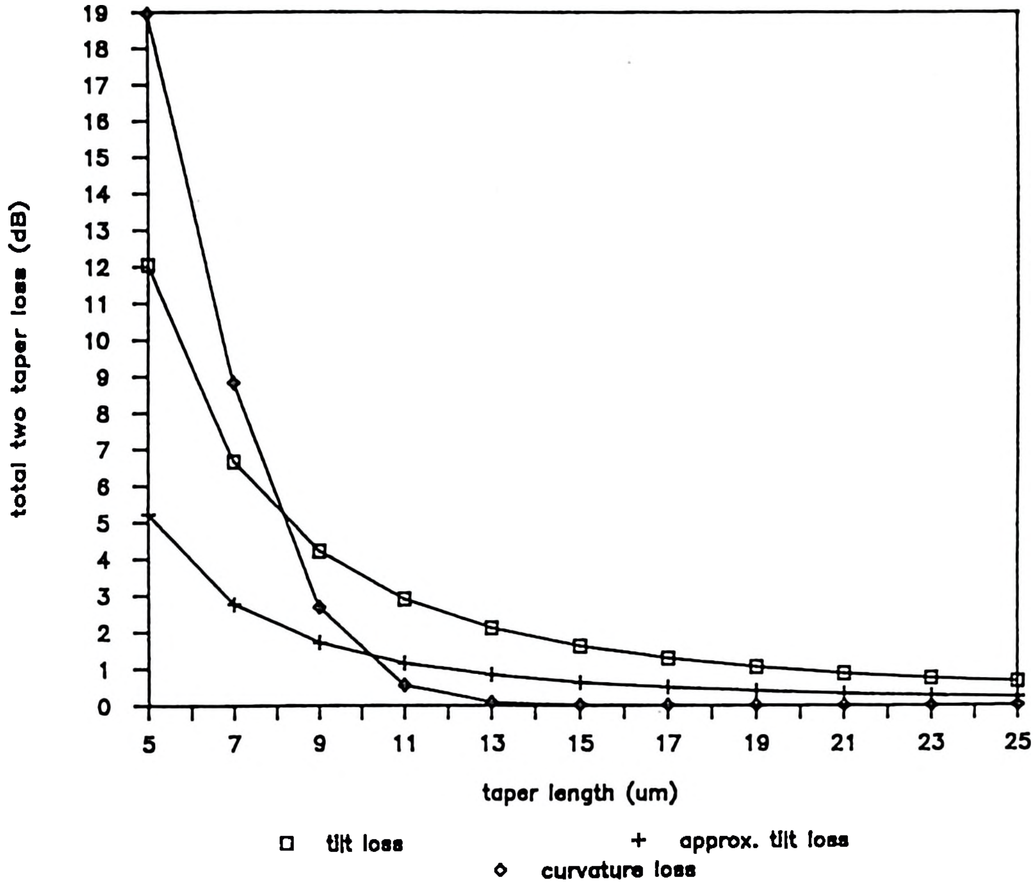

Figure 2.12 Taper insertion loss for two ideal tapers of Fig. 2.9(a)–(b).

index step, $n_1 - n_4 \approx 0.5$, but this air radiation does reduce the coupling efficiency. The case for the tilted waveguide is more complicated as one needs to calculate the coupling to the air and substrate radiation modes, where the power radiated into the air is lost. In preliminary fabricated tapers, the air radiation losses of short ($\approx 5\ \mu$m) and abrupt tapers were visibly observed to be large and the total two taper loss was $\approx$ 10 dB.

The above calculations are idealistic. The curved sections shown in Fig. 2.9 are strictly curved leaky waveguides, which have not been examined in the literature (and a detailed analysis here is beyond the scope of this work), but we are only interested in the approximate regimes of negligible curvature loss such that the leaky losses are dominant. Also, in a realistic taper the curvature will not be of a fixed radius and transition losses between sections of different radius of curvature (different β) may occur [33]. Similarly for any arbitrary taper shape, the propagation constant continuously changes as the cladding layer thickness decreases (Fig. 2.8) which also may cause transition losses

In the calculations for the linear tapers, equation (19) is not applicable to the leaky modes because they are unbound over the infinite cross–section and are not true power normalizable modes (although they can be "normalized" in the complex plane; see e.g. [33]). As mentioned previously, in the low loss case (large d) some of the leaky modes are akin to the true bound modes which have been used in the previous calculations: this is the case for the "upper tilt" of Fig. 2.9(b). For the "lower tilt" closest to the coupling region, the leaky loss is high and the leaky modes are quite different from the true normal modes (see e.g. Fig. 2.8). It is not obvious how the coupling loss for this leaky tilted waveguide can be calculated.

As explained in section 2.5, the taper shapes and lengths are not under stringent exact control so any errors brought about by the above idealizations are largely mitigated by this uncertainty. The important design rules are that the tapers should be much larger than 15 μm and be smooth gradual transitions with no abruptness.

The total leaky loss of the coupler has two components: the total loss in the coupling region which is simply calculated from the loss and L, and the total taper loss due to varying loss as d changes through the taper. The total loss in the tapers is taken into account by defining a "loss equivalent taper length" L_{et}, i.e. the length which when multiplied by the loss in the coupling region (section 2.3) has the same total loss as the taper, or for a linear taper,

$$L_{et} = \frac{\text{total loss in the taper}}{\text{loss(d)}} = \int_0^{L_t} \text{loss}(d+sz/L_t)\ dz/\text{loss}(d) \tag{21}$$

where loss(d) is the leaky loss as a function of d and since loss($d+s$)$\approx$0,

$$L_{et} \approx \int_0^{\infty} \text{loss}(d)\ e^{(-2p_o sz/L_t)}\ dz \approx L_t/2p_o s \tag{22}$$

where the approximate form of equation (3) for the dependence of loss on d is assumed.

Plotted in Fig. 2.13 is equation (22) for a=0.70 μm and s=1.8 μm. Note that the equivalent length varies slowly with the actual taper length, and is typically 3–5 μm for our tapers: the difference of 2 μm per taper is a small unknown compared to the typical coupling lengths of 25 μm to 70 μm in the devices tested in

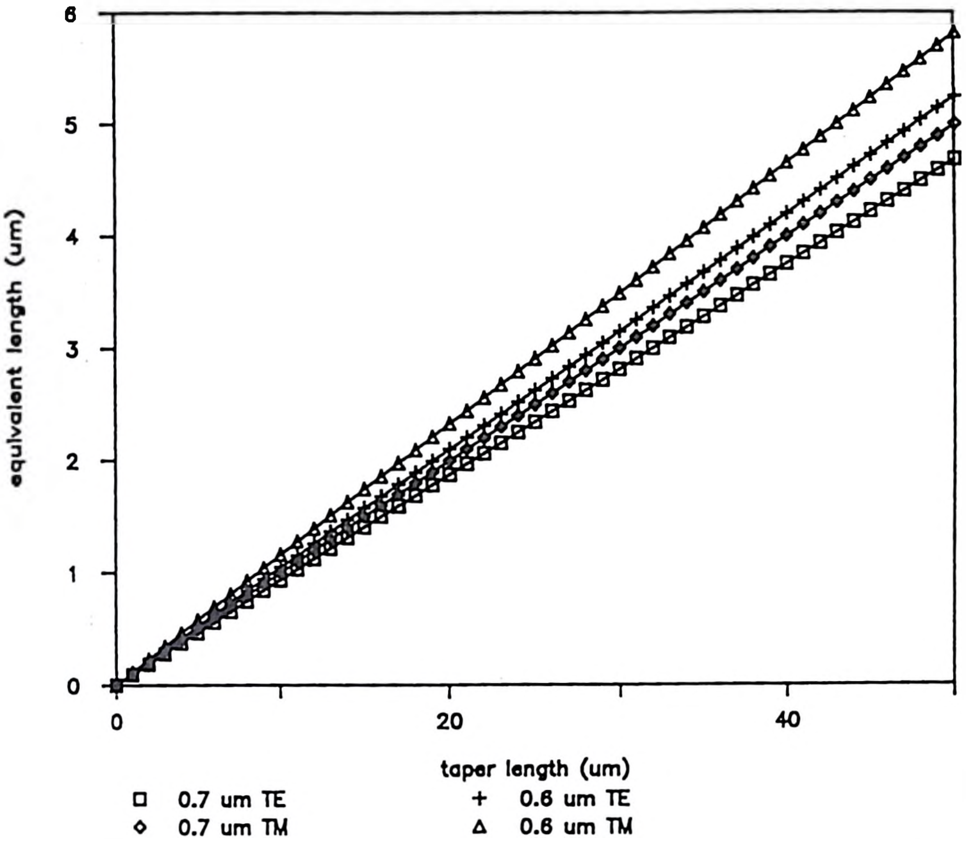

Figure 2.13 Loss equivalent taper length versus taper length.

section 2.5, with most devices at the larger end.

This section has been primarily concerned with the taper shape effect on the non–leaky losses. We briefly return to examine the effect of the tapers on mode conversion between leaky modes and the possible observable effects as discussed in section 2.3.

Plotted in Fig. 2.14 is the leaky mode propagation constants for the three–layer leaky waveguide (d=0) whose modal loss has been plotted in Fig. 2.3. An estimate of the spatial shape of a sinusoidally bent waveguide that would cause mode conversion is the well–known result from coupled–mode theory [41]

$$\beta_1 - \beta_2 = 2\pi/\Lambda \tag{23}$$

where Λ is the spatial period of a sinusoidal mechanical variation, and β_1 and β_2 are the propagation constants of the modes which convert between each other.

From Fig. 2.14 for a=0.6 μm the spatial period that would cause mode conversion between the TE_0 and TE_1 mode is 2.8 μm. This is an extremely abrupt taper transition length, which we have already decided should be avoided. This estimate of the taper discontinuity length that causes mode conversion does not predict the magnitude of the conversion, which is determined by the size of the discontinuity, the modal field overlap and the length of the interaction region (length of the taper). The above argument has been applied to a few structures with d>0 with the same conclusions.

The analysis of mode coupling in leaky structures is beyond the scope of this work, but the approximate justification above that gradual tapers should eliminate the coupling will be tested in the experimental section.

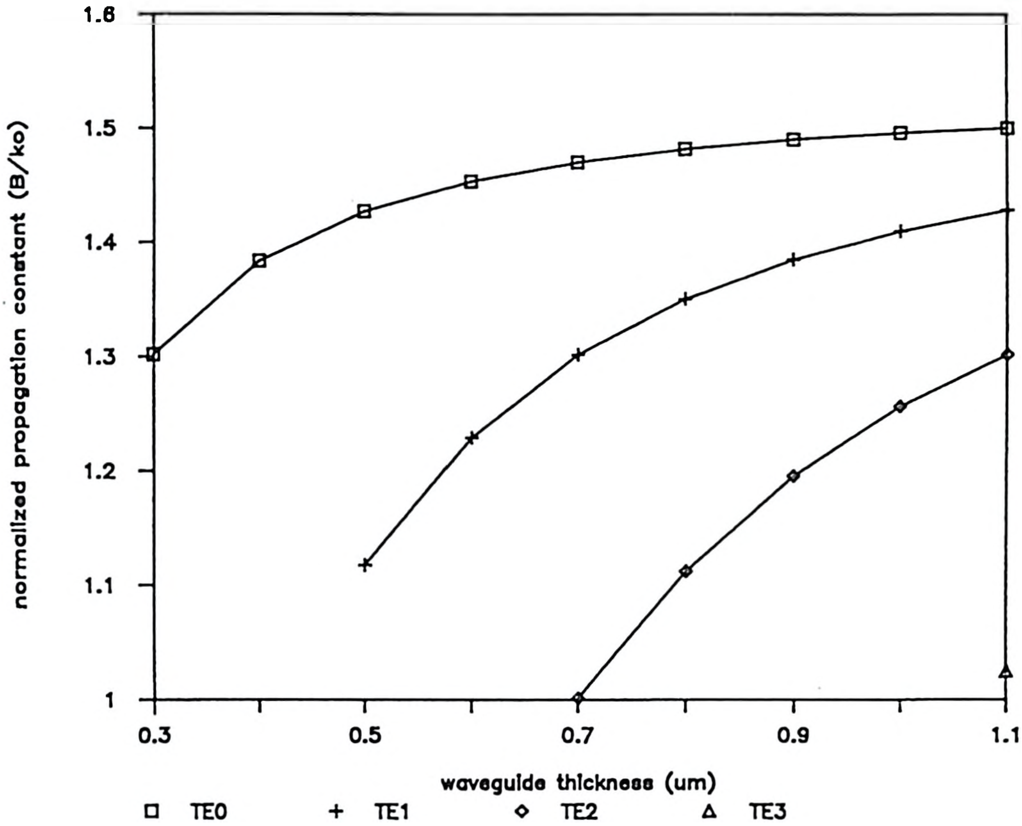

Figure 2.14 TE_0, TE_1, TE_2 and TE_3 normalized propagation constants for d=0.

2.5 Fabrication of Couplers and Measurement of Leaky Wave Losses

A set of couplers (i.e. an IWDC without the detector), were fabricated to confirm the leaky wave losses. Plotted in Fig. 2.15 is a scale drawing top view of a portion of the test mask set with an enlarged side/cross section view of a coupler with a traversing rib waveguide. The coupler lengths (of 9 μm, 18 μm, 27 μm and 54 μm; with only the latter two shown in Fig. 2.15) are also shown, but the fabricated devices were ofter larger because of the undercutting required to fabricate the tapers. The waveguides were 9 μm in width.

The devices were fabricated as follows. A 2 inch (100) silicon wafer was thermally oxidized in wet oxygen at $\approx$1100 ^{o}C for 8 hours yielding a typical SiO_2 layer thickness of 1.8 μm. To fabricate the coupler region with tapers, a photoresist mask was patterned by conventional photolithographic methods followed by etching (the unmasked coupler region) in 20:1 NH_4F:HF at 60 ^{o}C for 4–5 minutes until the SiO_2 was completely removed and gradual tapers formed [42]. The wafer was re–oxidized to the desired thickness d from growth charts and compared with thin film interference color charts [35]. A nominal 0.65 μm Corning 7059 glass waveguide was deposited on the cleaned wafer by magnetron–sputtering in a 1:1 Ar:O_2 ambient at a pressure of 3–4 mTorr at 100 W power. A typical sputter run began with a system base pressure of 4x10^{-7} T, a target pre–sputtering of 30 minutes followed by a deposition time of 6 hours. The sputtering apparatus has been discussed elsewhere [36] and magnetron–sputtering of Corning 7059 glass has been discussed in the literature [37]. Rib waveguides were patterned on the sputtered sample by photolithography and etched for 15–20 s in 6:1 NH_4F:HF at 40 ^{o}C. Typical rib heights were measured by a Tencor Alphastep surface profiler to be

Scale 6.75:1

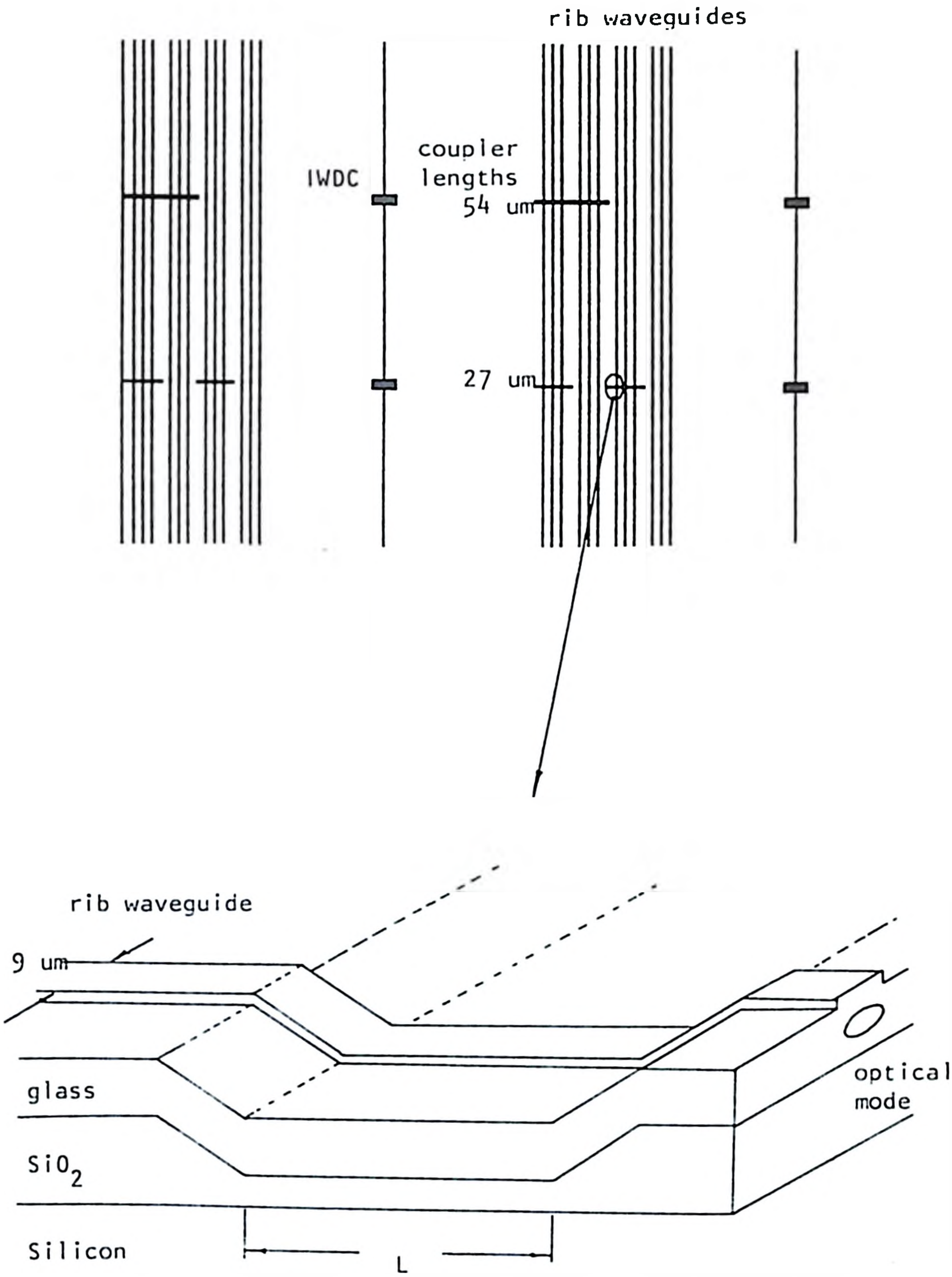

Figure 2.15 Top view of composite mask set for the couplers.

0.10–0.12 μm. Before testing, the sample was carefully cleaved on both ends to facilitate end–fire coupling into the waveguides. This was not easy as silicon is a difficult material to cleave, but satisfactory cleaves were nonetheless obtained, as observed visually by scanning electron microscopy (SEM) and by observing the quality of the slab waveguide mode near–field..

Fabricated taper slopes were 20–40 μm long for a change in SiO_2 thickness of about 1 μm (by observing the interference fringes of the tapered SiO_2), with gradual curved transitions. The glass and SiO_2 thicknesses were confirmed by SEM cross–sections of cleaved and carbon–coated devices. Shown in Fig. 2.16 is a SEM photograph of the glass/SiO_2/silicon layers. The correct identification of the layers was confirmed by compositional analysis using energy dispersive x–ray analysis (EDX). For example, the silicon substrate had the highest silicon count followed by the SiO_2 and the glass. The silicon and SiO_2 contained no other heavy atoms, while the glass had an aluminum and barium peak which is consistent with the composition of 7059 glass (50.2% SiO_2, 25.1% BaO, 13% B_2O_3, 10.7% Al_2O_3, 0.4% As_2O_3).

Shown in Fig. 2.17 is a side/edge view of a coupler with a traversing rib waveguide (similar to the cross–section inset of Fig. 2.15). Fig. 2.18 is a photograph of a cross–section of a single (short) taper showing the gradual transitions and Fig. 2.19 is a photograph of a cleaved end of a rib waveguide.

Prism–coupling at $\lambda = 0.6328$ μm using a Schott glass SF6 prism with an index of 1.80 (1.805 at λ=557.56, 1.79609 at λ=656.2725) was used as a waveguide characterization tool to determine the sample thickness and refractive index. It was also used to determine the refractive index of the SiO_2 given the SEM

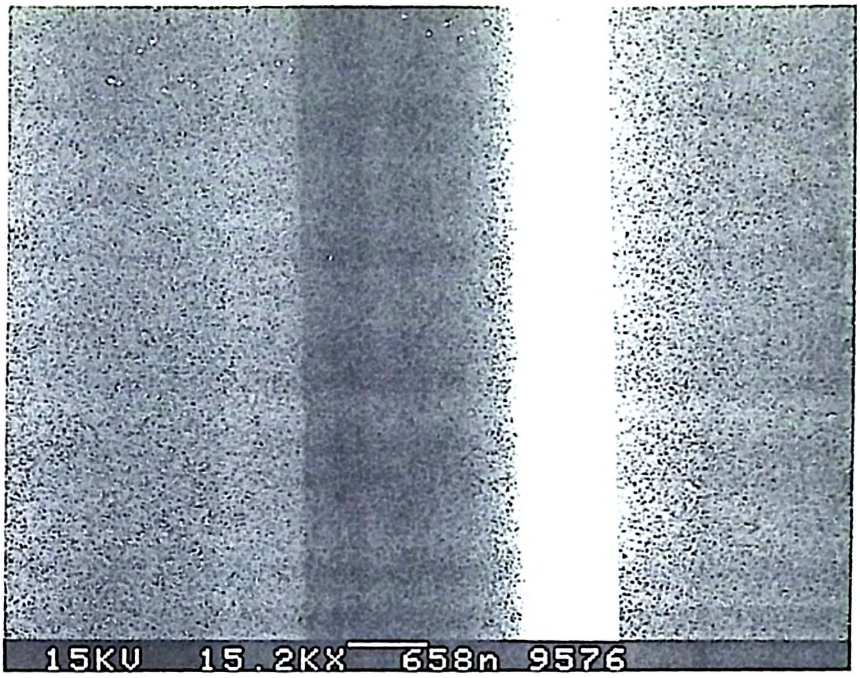

Figure 2.16 SEM cross–section of glass/SiO_2/silicon layers.

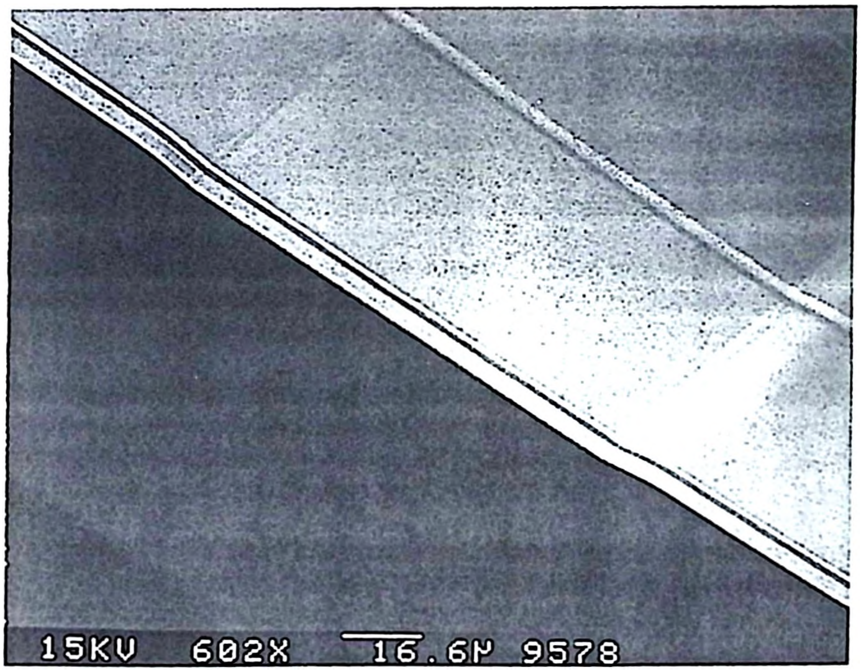

Figure 2.17 Side/angle view of a rib waveguide traversing a coupler.

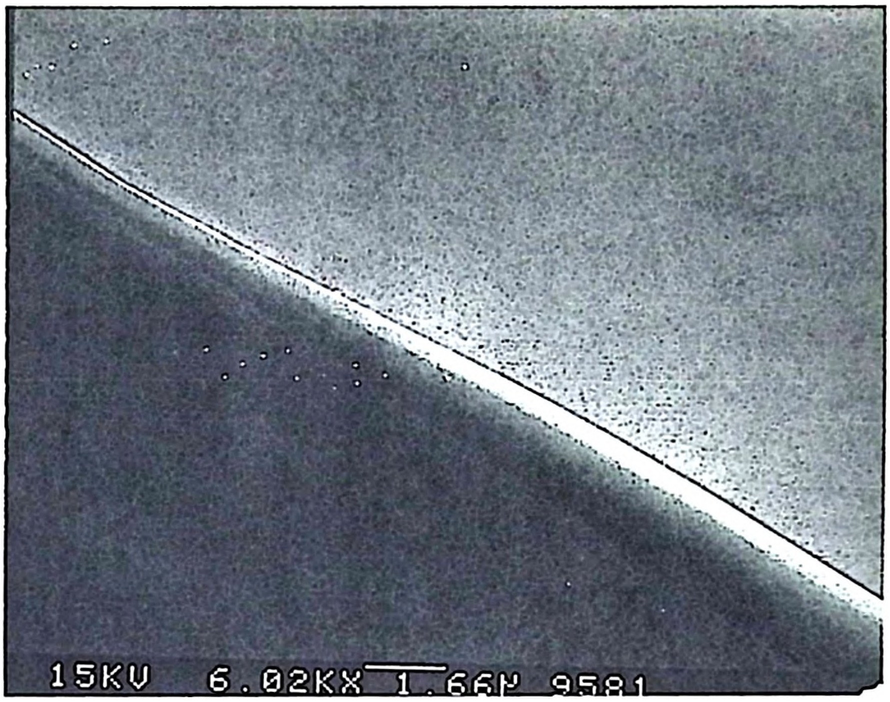

Figure 2.18 SEM cross–section of a (short) taper.

Figure 2.19 SEM cross–section of a cleaved edge of a rib waveguide.

measured glass thickness. The details of prism coupling has been discussed elsewhere (see e.g. [2]). Once the SiO_2 refractive index is known, the prism method can measure the waveguide thickness to better than a random error of 5 percent and the refractive index to better than 0.03 percent. Our knowlege of the accuracy may be limited by variations of the sample thickness because in principle higher accuracies are possible [2]).

The waveguides used in this study are essentially single–mode (as the higher order leaky modes have high loss), thus the thickness and refractive index can only be determined by measuring the TE and TM coupling angles, with the tacit assumption of an isotropic non–birefringent material. Jeromenik et al. [37] have seen a birefringence of $2–3\times10^{-3}$ for 1:1 $Ar:O_2$ ambient magnetron–sputtered samples, probably due to stress in the as–grown film. We have sputtered a thick waveguide sample (1.64+.02 μm measured by SEM) which supports at least two mode orders (in TE and TM) to determine the birefringence and the glass and SiO_2 refractive indices. The glass and SiO_2 refractive indices were determined to be 1.5240±.0005 and 1.464±.004, respectively; in agreement with the literature [11,19,37]. The film birefringence is $\approx 8\times10^{-4}$.

The total loss of a coupler is defined as

$$\text{total loss (dB)} = 10\log(P_o/P_{tc}) \tag{24}$$

where P_o and P_{tc} is the power measured out of an open waveguide and out of a waveguide which traverses a coupler, respectively, given the same input conditions and identical waveguides (i.e. the same loss).

The apparatus for measuring P_o and P_{tc} is illustrated in Fig. 2.20.

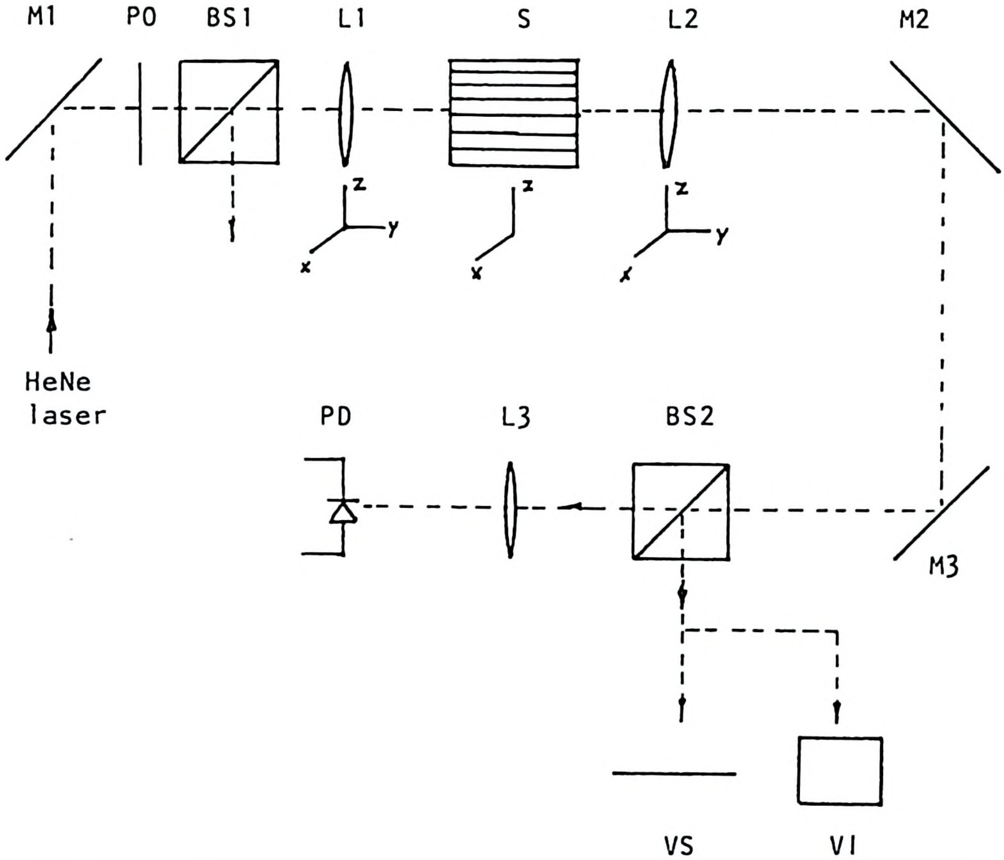

Figure 2.20 Experimental apparatus for measuring the leaky losses.

The HeNe laser is reflected by a mirror (M1) for directional control then polarized by a sheet polarizer (PO) and incident on the input 20X microscope objective (L1) mounted on a micropositioner with a y–axis piezoelectric translator (PZT). The laser beam is focused onto the input cleaved facet of the sample (S) which is mounted on a micropositioner with a z–axis PZT. The output waveguide mode near–field pattern of the sample is imaged by the 20X microscope objective (L2) onto a viewing screen (VS) or vidicon (VI) over a length of 5 meters for high magnification (via M2, M3 ... M5) and partially reflected by a beamsplitter (BS2). The input focused spot can be monitored by examining the retro–reflection from the sample input facet with the pellicle beam splitter (BS1). The total optical power propagating out of the waveguide is measured by focusing the back facet near–field image onto a Photodyne model 66XLA optical power meter (PD) by a lens (L3). This apparatus allows monitoring of the output power and visual confirmation of the waveguide coupling and output near–field quality. The long magnification path spatially filters the slab guided light so only the guided power is measured at PD, although an optional iris aperture may be necessary for short samples and/or short paths (see e.g. [22]).

The apparatus is preliminarily aligned by affixing a microscope glass slide on the thread–end of the objective L1 and adjusting the laser beam such that it is retro–reflected: this aligns the lens' optic axis with the laser. After mounting the sample the HeNe is focused on the front cleaved facet of the sample and the waveguide position is adjusted until coupling is achieved. The output power is maximized by successive optimization of the input beam angle (through M1) and adjusting the lateral, transverse and longitudinal position of the waveguide relative to the focused spot.

A typical measurement of a coupler involves measuring P_{tc} for three waveguides of the coupler and P_o for the three waveguides of the open waveguides (Fig. 2.15) and the total loss is obtained from averaging the results. The process is repeated for all devices on the wafer. The loss is determinloss by the coupler length L measured by a calibrated optical microscope and adding $2L_{et}$ for the tapers (≈8 μm). The sample is removed and the "corrected input power" is measured where the mirror and lens losses are taken into account, to determine the insertion loss of the open waveguides and thus the propagation loss of the waveguides if the input coupling loss is known. For each wafer, both TE and TM measuremenmts were made.

So far it has been tacitly assumed that the rib waveguides used to experimentally measure the leaky losses is a trivial extention of the slab case discussed in section 2.3. In the general case, the leaky losses of two–dimensional waveguides (with both slab or transverse and lateral confinement) is not the same as the slab waveguide equivalent of the rib region. This can be seen from the exact modal field solution of strongly laterally confined rib waveguides as compared to the "slab" approximate solutions (the effective index method) [50]. This creates two possible problems: the transverse field profile in the rib (region 1, Fig. 2.21(a)) may not be the same as the slab (if the rib were infinitely wide) due to "mode squeezing" by the rib (Fig. 2.21(b)), and the mode power not confined under the rib has a higher leaky loss because the waveguide is thinner. These errors are avoided in our waveguides which are weakly laterally guided, with a small rib height (0.10–0.12

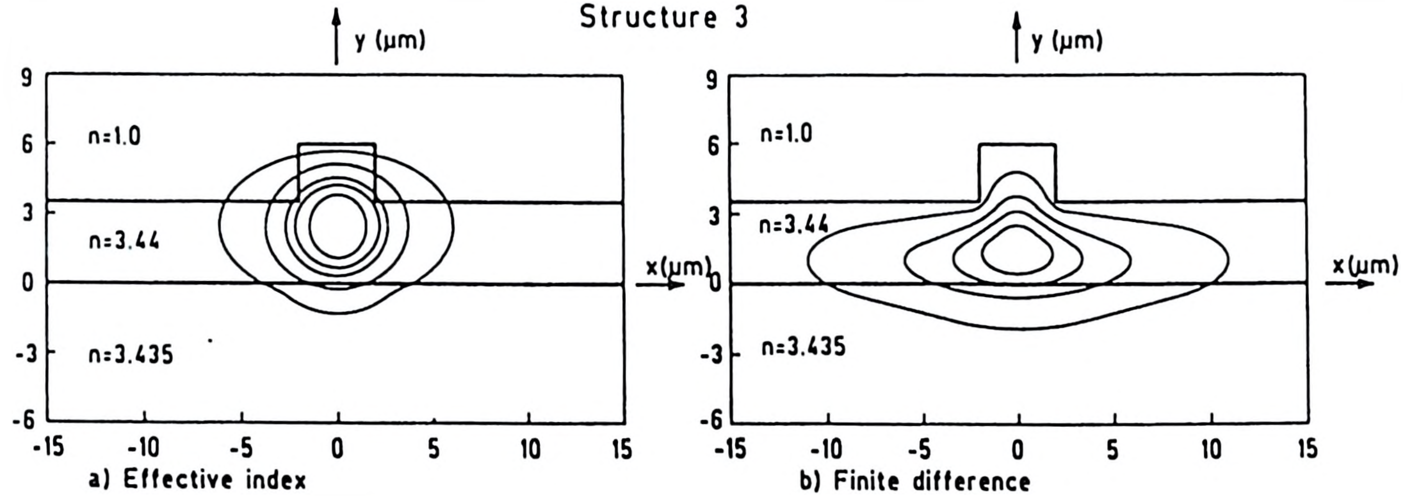

Figure 2.21 Electric field contours of a strongly laterally confined rib waveguide solved by the approximate "slab" effective index method (a) and exact numerical finite difference method (b) (from [50]).

μm) compared to the waveguide thickness (0.60–0.70 μm) and a large rib width to waveguide thickness asymmetry ratio ($\approx$14). As a result (for power propagating in the rib) the rib waveguide is equivalent to the slab and the mode is laterally well–confined in the rib as calculated (see e.g. [50]) and observed experimentally (Fig. 2.22(a)–(b)).

2.6 Results

Several devices on eight wafers (samples 106,107,109,111,113,115,119 and 120) were measured with SiO_2 thicknesses of 0.15 μm to 0.8 μm (0.15 μm to 0.4 μm for TE and 0.15 μm to 0.8 μm for TM. For almost all samples the waveguide thickness was between 0.6 μm and 0.7 μm. A summary of all measurements is tabulated in Table 1. The errors in the measurements for the coupling loss of each device is defined as the standard error $\sigma/\sqrt{N}$ where σ is the standard deviation of the measurements in each group and N is the number of measurements (generally 3 or 6). Several devices on each wafer were measured and then averaged.

The errors in the loss tabulated in Table 1 are statistical errors from averaging several separate measurements, generally, each coupler measurement has an error of 30–40 percent due to a 0.3–1.0 dB scatter in each group of waveguide measurements. This is much larger than expected from experimental measurement errors alone which are $\lesssim$ 0.3 dB and in fact on most samples the waveguides within a group were remeasured two or three times. The scatter is no less acute for open rib waveguides compared to couplers so we assume it is inhomogeneous loss from variable cleave quality and/or waveguide imperfections. The latter is most likely as coupling efficiency measurements (see below) on short (1–1.5 mm) samples were

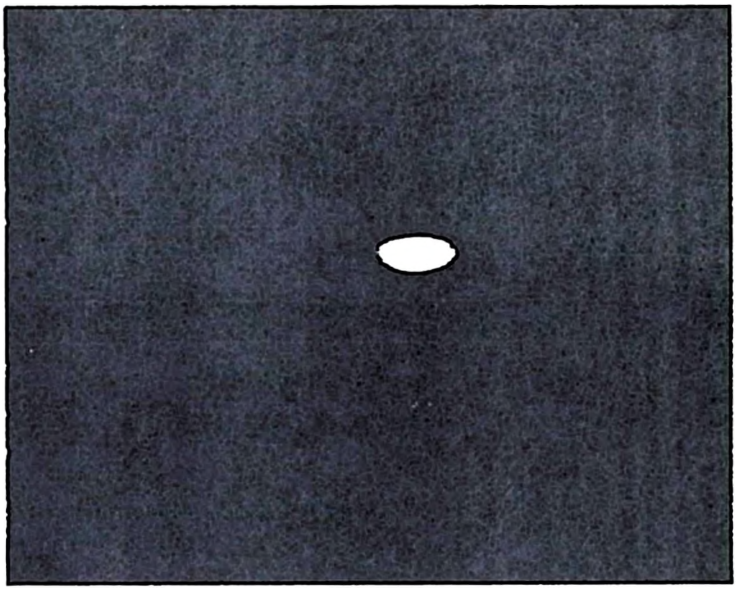

(a)

$5\,\mu m$

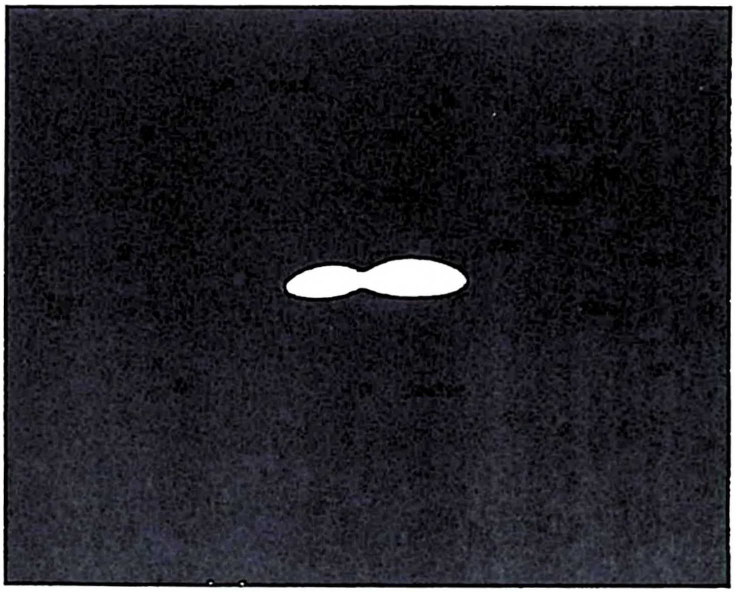

(b)

Figure 2.22 Waveguide mode near–field pattern for the TE_0 modes, lowest order lateral mode (a) and second order (and only higher order) lateral mode (b).

Table 1 Summary of coupler leaky loss measurements.

sample	SiO_2 thickness (um) (±.016 um)	glass thickness (um) (± 5%)	TE$_0$ loss (dB/cm)	number of measurements (TE)	TM$_0$ loss (dB/cm)	number of measurements (TM)	waveguide propagation loss (dB/cm)
111	0.157	0.85	1520±26	8	5850±48	2	2.7±0.3
107	0.200	0.68	1225±75	4	5705±440	2	2.8±0.5
113	0.250	0.70	1024±51	6	4787±126	2	4.8±0.4
109	0.282	0.60	834±37	7	3478±64	3	4.7±0.5
115	0.360	0.57	535±42	6	3028±64	4	2.6±0.7
106	0.423	0.60	446±30	14	1267±123	2	3.5±0.7
119	0.579	0.69	-	-	753±122	4	3.7±0.3
120	0.815	0.69	-	-	361±106	3	3.5±0.8

uniform to within 0.2 dB, whereas for long waveguides (> 1 cm) light guided in the waveguide is readily visible as surface scatter and the scattering is not uniform along the waveguide. Inspection of the waveguides under an optical microscope shows common breaks and processing imperfections on the ribs. Nonetheless, these problems are largely averaged by the increase in statistical accuracy from a large number of measurements.

The propagation losses of the waveguides were determined by subtracting the coupling loss from the total insertion loss of a length of waveguide then dividing by the length; typical values are 3–5 dB/cm.. The coupling loss was determined by measuring the insertion loss of very short (1–1.5 mm) samples and taking the average value as the input coupling loss only, which was found to be 6.0 dB ± 0.2 dB. We reiterate that in Table 1, the TE and TM loss tabulated in the fourth and sixth columns are the leaky losses <u>in the coupling region only</u>, whereas the propagation loss tabulated in the last column is for the "normal" waveguide (A, Fig. 2.1).

The experimental leaky wave loss results are plotted in Fig. 2.23 with the theoretical results for 0.6 μm and 0.7 μm waveguide thickness. The results are in good agreement with theory. The theoretical results are accurate to about 20–35 percent (the error bars plotted in Fig. 2.23) given the uncertainty in the SiO_2 refractive index (±0.004) which contributes an error of typically no more than 20 percent for SiO_2 thicknesses upto 0.8 μm, and the uncertainty in the waveguide thickness of 5 percent with an error of ≈15 percent. In addition we use 3.88 as the real index of silicon [20], but some authors have used 3.85 [38]: this introduces an additional error of only $\lesssim$1 percent.

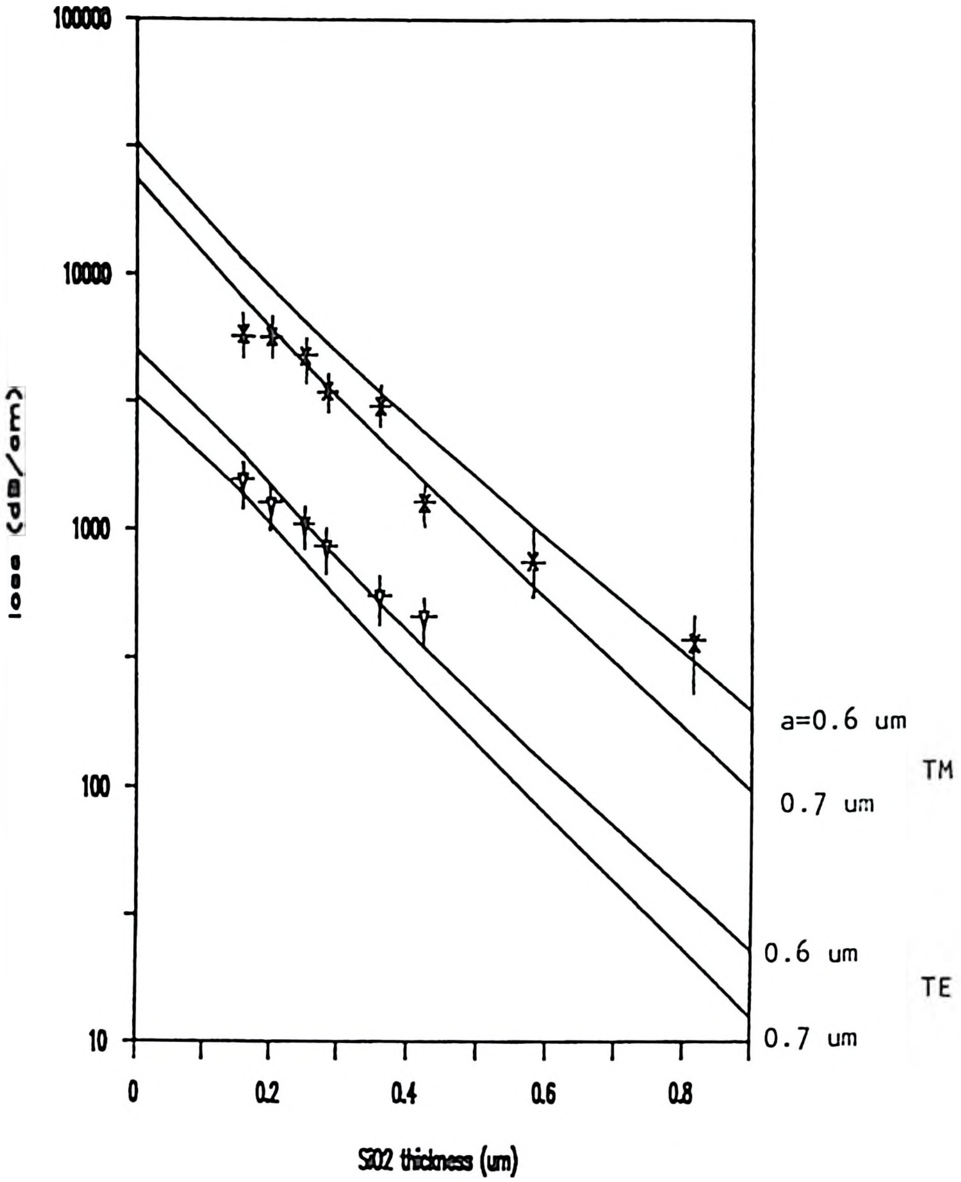

Figure 2.23 Experimental and theoretical leaky wave losses at λ=0.6328 μm.

It was anticipated that the experimental TM results would be smaller than expected from theory because of side–wall roughness induced depolarization in the rib waveguides [39–40]. For example, if the TE loss is 1000 dB/cm and the TM loss is 7000 dB/cm, for a coupling length of 50 μm and a depolarization of one percent the measured TE and TM loss is 1009 and 4918 dB/cm, respectively.

Depolarization in several open waveguides on each sample were measured and the results are tabulated in Table 2. The depolarization over typical lengths of 1.2 to 1.4 cm was as large as 25 percent (corresponding to an output TE/TM or TM/TE power ratio of 3 for a single TM or TE polarization input) and typically 0.7 percent. But these meaurements were for propagation over the full edge–to–edge length of the wafer whereas the distance from the wafer edge to the couplers was obviously less. The depolarization increases as the square of the distance propagated in the waveguide, thus the effective depolarization at the coupler is smaller than the full wafer length value (Table 2); typically 0.1–0.3 percent which for the example above results in only a 9–17 percent error in measuring the TM loss which is within the experimental error. In some samples there was a noticeable TE–in and TM–in depolarization anisotropy which is in qualitative agreement with that seen by Garmire et al. [39] because of the larger TE loss induced by the side–wall roughness. The above depolarization results have been corrected for the small depolarization in the focusing optics (0.35 percent) and a polarization dependent mirror reflectivity. The polarization leakage of the sheet polarizer is small (0.04 percent).

The TM leaky wave measurements are in good agreement with theory, but for the tapered IWDCs used in this work it is possible that there is

Table 2 Depolarization of rib waveguides.

sample	TE-in TE/TM ratio of output power	TM-in TM/TE ratio of output power
107	21	46
109	140	250
111	100	-
113	276	211
115	123	114
119	-	114
120	-	3

TE-in

effective TE/TM ratio of power at first coupler	second coupler
230	-
858	384
502	192
954	-
1518	379
744 *	224 *
15 *	-

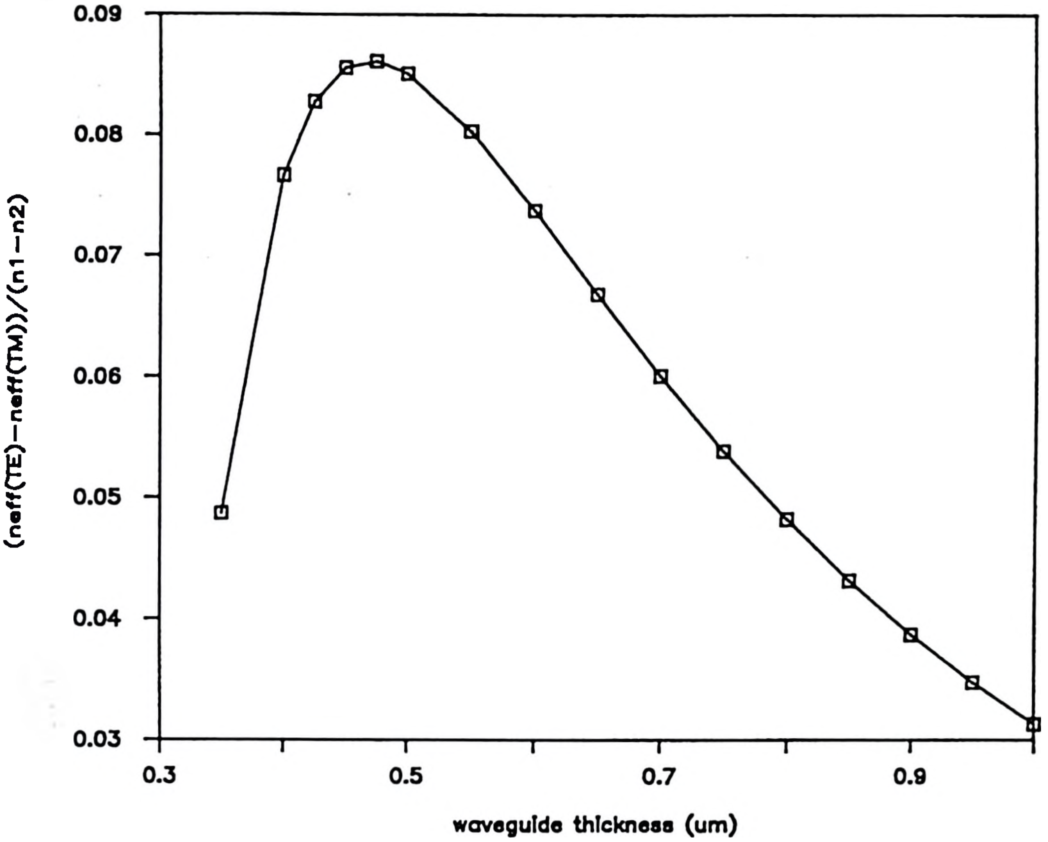

Figure 2.24 $(\beta_{TE}-\beta_{TM})/(n_1-n_2)k_o$ versus waveguide thickness for non–leaky three–layer waveguide ($d\rightarrow\infty$).

depolarization in the tapers because of the nearly degenerate TE and TM modes of the waveguide. Plotted in Fig. 2.24 is the difference in propagation constant of the TE_0 and TM_0 mode versus waveguide core thickness of the three–layer non–leaky waveguide ($d \to \infty$). From equation (23) the spatial period Λ that may cause depolarization is 160 μm to 180 μm, which is larger than the typical taper lengths, but of similar order. Unfortunately, it is experimentally impossible to delineate the waveguide depolarization from the taper depolarization. It is possible that if the depolarization in the tapers becomes a dominant mechanism that a minimum taper length may exist to minimize it.

Note, there is no TE–TM mode conversion in a slab waveguide because the electric field vectors are identically orthogonal, as opposed to the general 2D waveguide where the TE and TM modes are coupled by the longitudinal field components [39]. For weakly laterally guided 2D waveguides these longitudinal field components are small (hence the good accuracy of the slab effective index approximations [26]) and the mode coupling is weak. Remember, equation (23) only roughly determines the perturbation shape which causes mode conversion and not the strength.

CHAPTER 3

INTEGRATED WAVEGUIDE–DETECTOR COUPLERS AND APPLICATIONS TO OPTOELECTRONIC SWITCHING

3.1 Introduction

In the previous Chapter, the leaky wave losses of the coupler were found to be in agreement with theory. We are now confident to design integrated waveguide detector–couplers (IWDCs) with particular application to a 2X2 optoelectronic switch.

3.2 Introduction to Optoelectronic Switching and the Topology of a 2X2 Switch

An optoelectronic switch matrix (Fig. 3.1) using photodetectors as switching crosspoints has been proposed for frequency division multiplexed television switching [43]. In this type of switch (say an NxN) N optical input signals, where each input channel distributes light to N detectors by passive splitters, can be switched to N electrical output channels by turning on/off the appropriate photodetector crosspoints. This approach is in contrast to all–optical switching schemes for broadband switching which have been of recent strong research interest [9]. The optoelectronic scheme is functionally equivalent, except for the OE conversions at the detectors and EO conversions are required for an optical output. The architecture of the optoelectronic switch is similar to that proposed for optical switches [54] and is strictly non–blocking and has a broadcast capability.

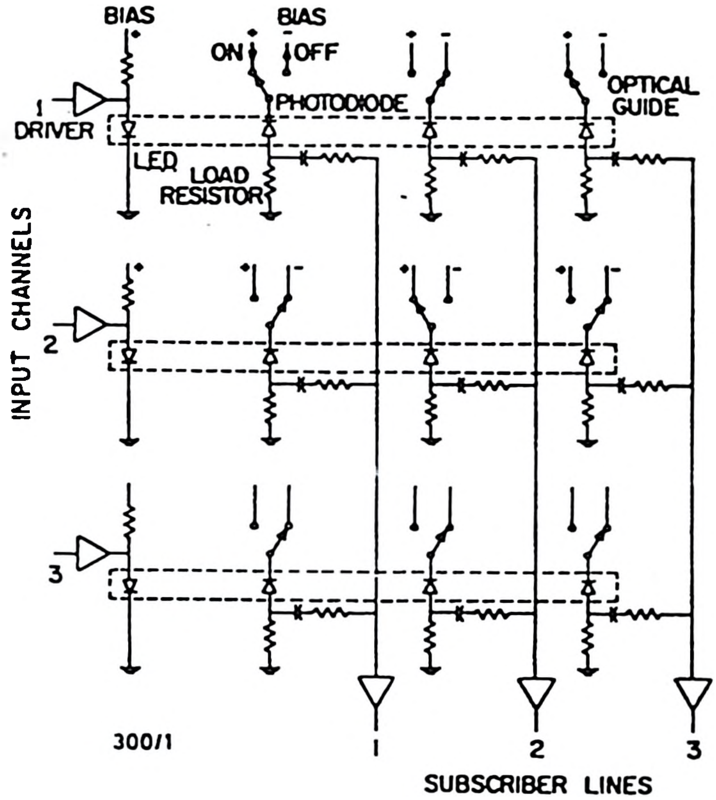

Figure 3.1 3X3 optoelectronic switching matrix (from [43]).

The first optoelectronic switching proposal [43] examined silicon p–i–n detectors as switching elements where reverse–bias turns–on the detector (switching crosspoint) and forward–bias turns–off the detector. Recently, silicon p–i–n detector matrices for optoelectronic switching has been discussed in detail [44]. It has been found that at 100 Mb/s (NRZ) with an optical input of 0 dBm and stray capacitance $\leq$ 1 pF that matrix dimensions of better than 100x100 are possible. Although a p–i–n detector has superior noise performance, the switch reconfiguration speed (detector on/off time) is slow because of the storage time of the large forward–bias capacitance, typically 1 μs. This latter figure is to be compared to $LiNbO_3$ directional coupler all–optical switches with > 1 GHz switching bandwidth [45]. In terms of physical size, detector active areas can generally be made small, $\leq$ 100 μm dimensions (see below), compared to the millimeter interaction length of a directional coupler based optical switch. For example in the literature, an 8x8 $LiNbO_3$ directional coupler optical switch matrix is 6 cm long [9]; a 100x100 switch would be roughly 72 cm long!

For high speed switching and small size, monolithic arrays of GaAs photoconductors have been demonstrated as optoelectronic crosspoints [46–47]. A switch reconfiguration speed of ≈ 1 ns, broadband response (> 1.3 GHz) and large isolation of better than 70 dB has been achieved. The (detector) isolation is defined as the ratio of photocurrent when the detector is on compared to off. The active area detector sizes varied from only 5 μm^2 to 20 μm^2, allowing a potentially large crosspoint density. In general, the noise performance of a photoconductor is not as good as a p–i–n detector at the highest bit–rates, so the 100x100 switch dimension may be optimistic, but gain with high bandwidth is possible, for example InGaAs photoconductors with a gain bandwidth product of 125 GHz has been demonstrated [49].

An experimental 3x3 optoelectronic switch using optical fiber, fiber splitters and surface illuminated discrete detectors has been demonstrated [48] and a monolithic version with integrated optical waveguides, splitters and detectors has been proposed. The monolithic integration of the optoelectronic matrix would potentially permit a large crosspoint density and simplified optical coupling to the switch as the number of fiber interconnections would be reduced by N^2–N compared to the discrete version. As described in Chapter 2, the IWDC (Fig. 3.2) has the unique property of providing power splitting and detection within the same physical space so a monolithic optoelectronic switch can be fabricated with the smallest possible size, i.e. the space requirements and 2–D interconnect problem of integrated passive waveguide splitters is eliminated.

The topology of a 2x2 switch using four IWDCs is shown in Fig. 3.3. The optical inputs 1 and 2 are switched to the electrical outputs 1 and 2 by the detector crosspoints controlled by the switching bias voltages V_1, V_2, V_3 and V_4.

The key figures of merit of an optoelectronic switch are the crosstalk between the channels, the detection bandwidth of the switch and the reconfiguration (detector on/off) time: in this work only the former two will be considered. The crosstalk originates from two mechanisms: the photogenerated carrier diffusion current noise from an adjacent detector and the finite isolation of each detector. The bandwidth of the detector is dependent on the photoconductor size and material parameters such as the carrier lifetime, mobility or saturation velocity.

The equal division of power amongst the detector crosspoints for each

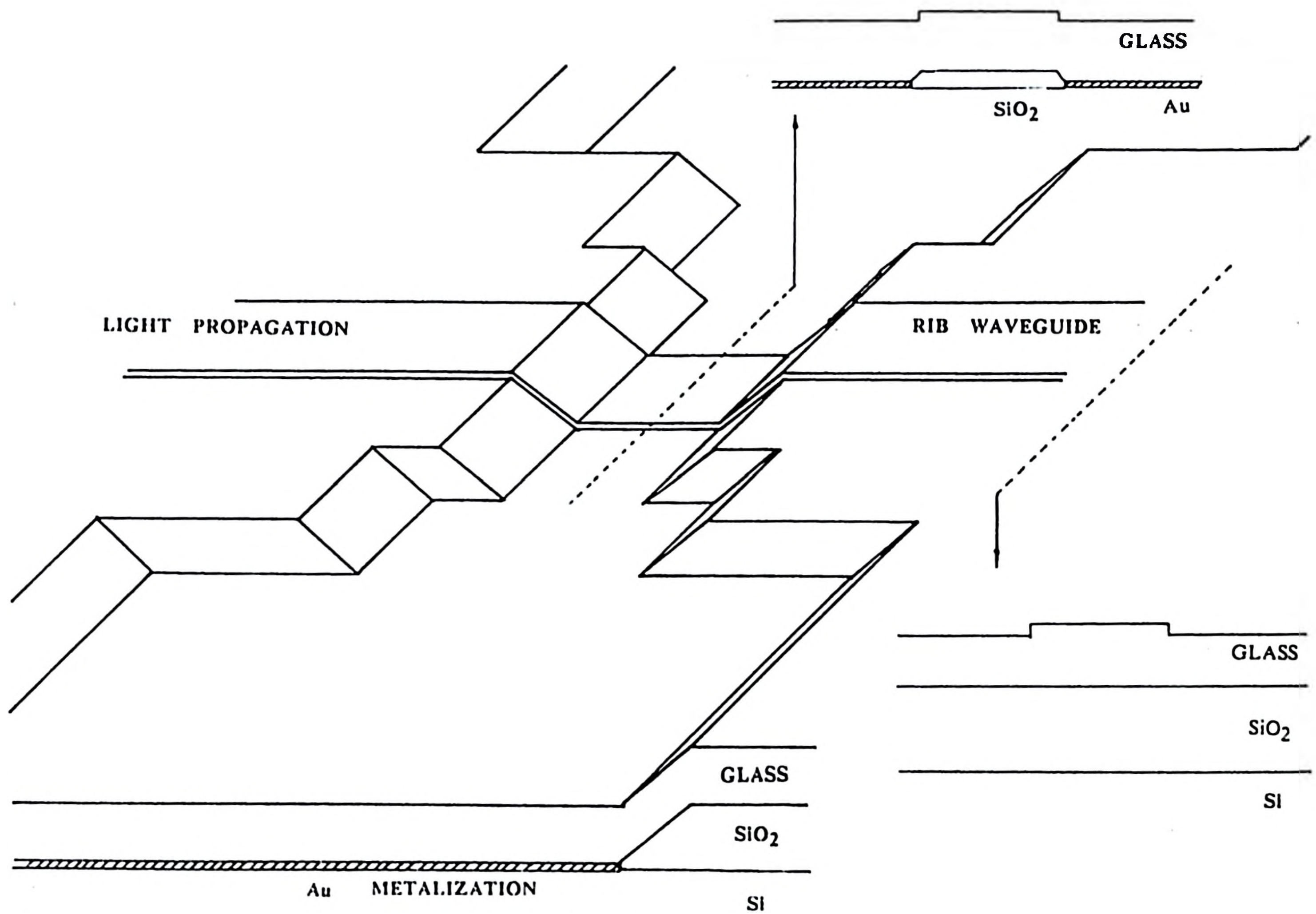

Figure 3.2 Integrated waveguide–detector coupler (IWDC).

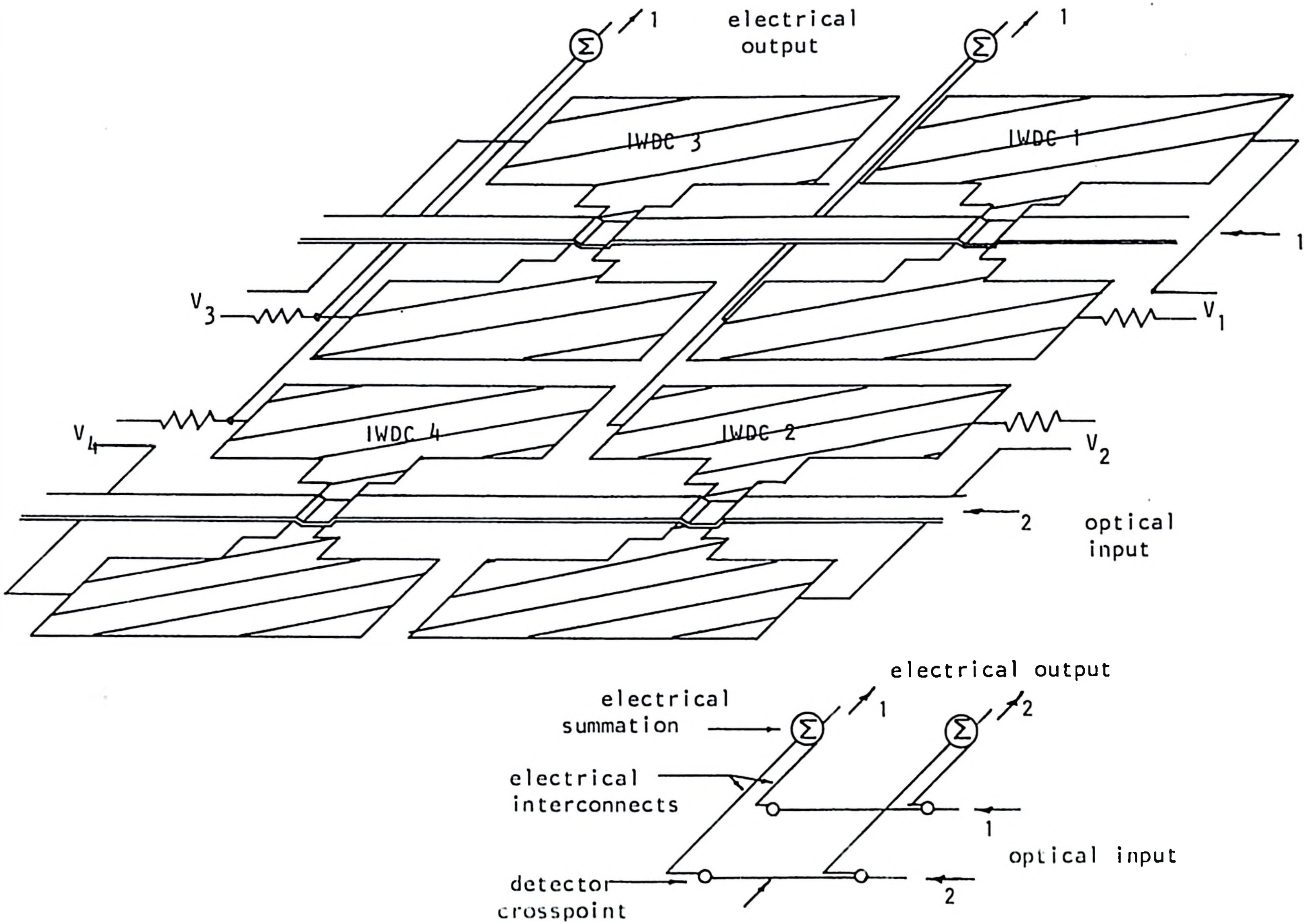

Figure 3.3 Topology of a 2X2 optoelectronic switch matrix using IWDCs.

optical input channel is important for maximum switch performance when the switch size and/or bit–rate is limited by signal–to–noise considerations: the switch performance will be limited by the worst crosspoint which receives the least optical power. Using the leaky losses determined in Chapter 2, the IWDCs can be designed for equal power coupling between all the detectors. For non–critical applications, any variation from equal power distribution can be re–normalized to some degree by voltage tuning the responsivity.

3.3 Device Fabrication and Testing

The three levels of the mask set required to fabricate the IWDCs and 2X2 switch are the SiO_2 window for the IWDC coupling region and detector electrodes (level 1; Fig. 3.4 and Fig. 3.5(a)), the detector metalization (level 2; Fig. 3.4 and Fig. 3.5(b)) and the rib waveguides (level 3; Fig. 3.4 and Fig. 3.5(b)).

There are "blocking" trenches (Fig. 3.4 and Fig. 3.5(a)) preceeding all the devices to absorb slab guided light and prevent subsequent erroneous detection as only the rib guided light is important. The detector pads and blocking trenches are placed equidistant such that the diffusion current crosstalk between the detectors, and between the detectors and the blocking trenches are equal and small (see below). Also, the detector gap of 40 μm is larger than the 15–20 μm gaps used in previous work at McMaster. The gap was increased to allow easier waveguide alignment because the 40 μm gap is decreased due to tapering of the SiO_2 when re–opening the SiO_2 after the re–oxidation (see below).

From the leaky wave calculations, the lead detector coupling length of 40 μm should result in a 3 dB IWDC for an SiO_2 thickness of $\approx$0.4 μm. The trailing

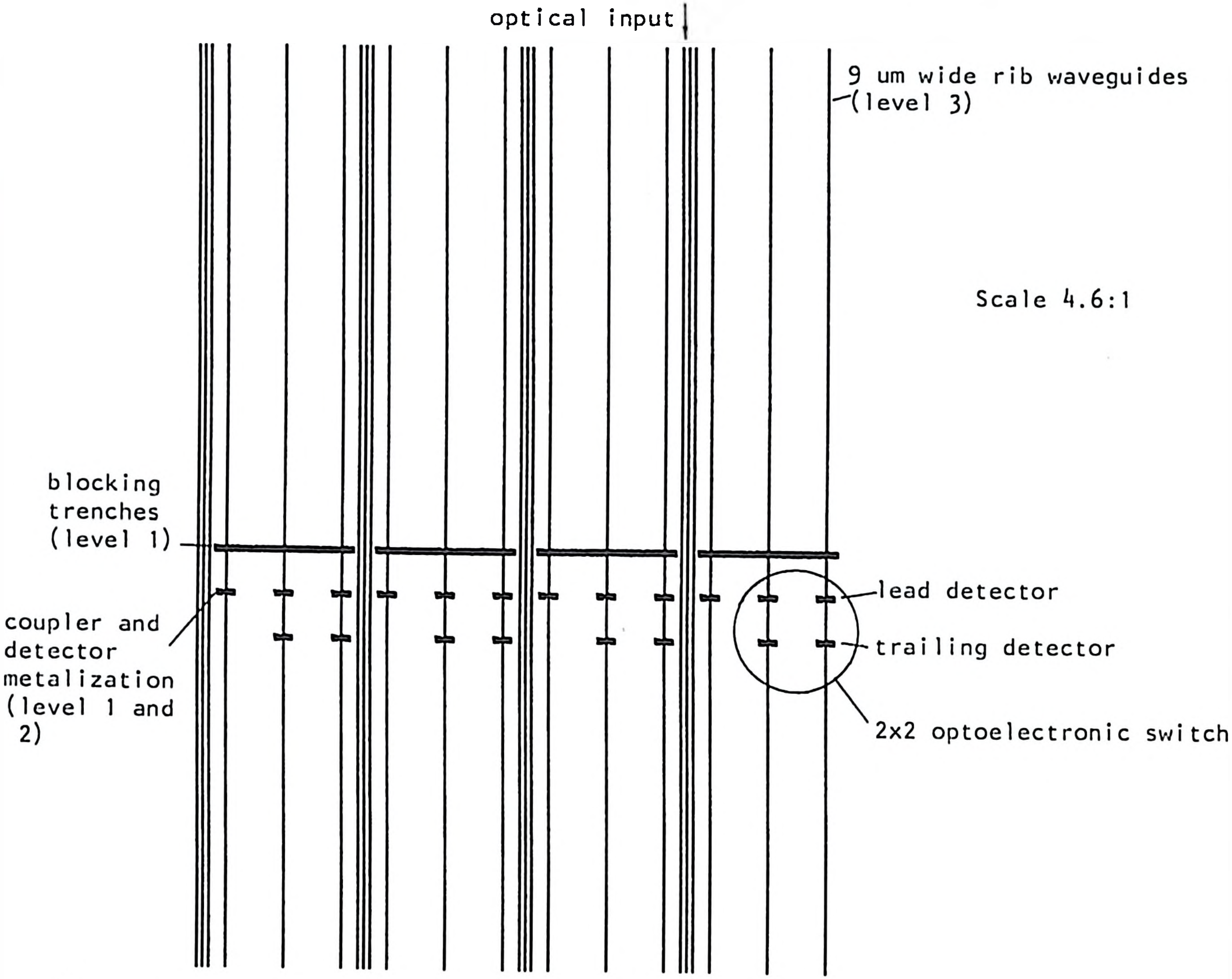

Figure 3.4 Top view of composite mask set (level 1, 2 and 3) for 2x2 switches.

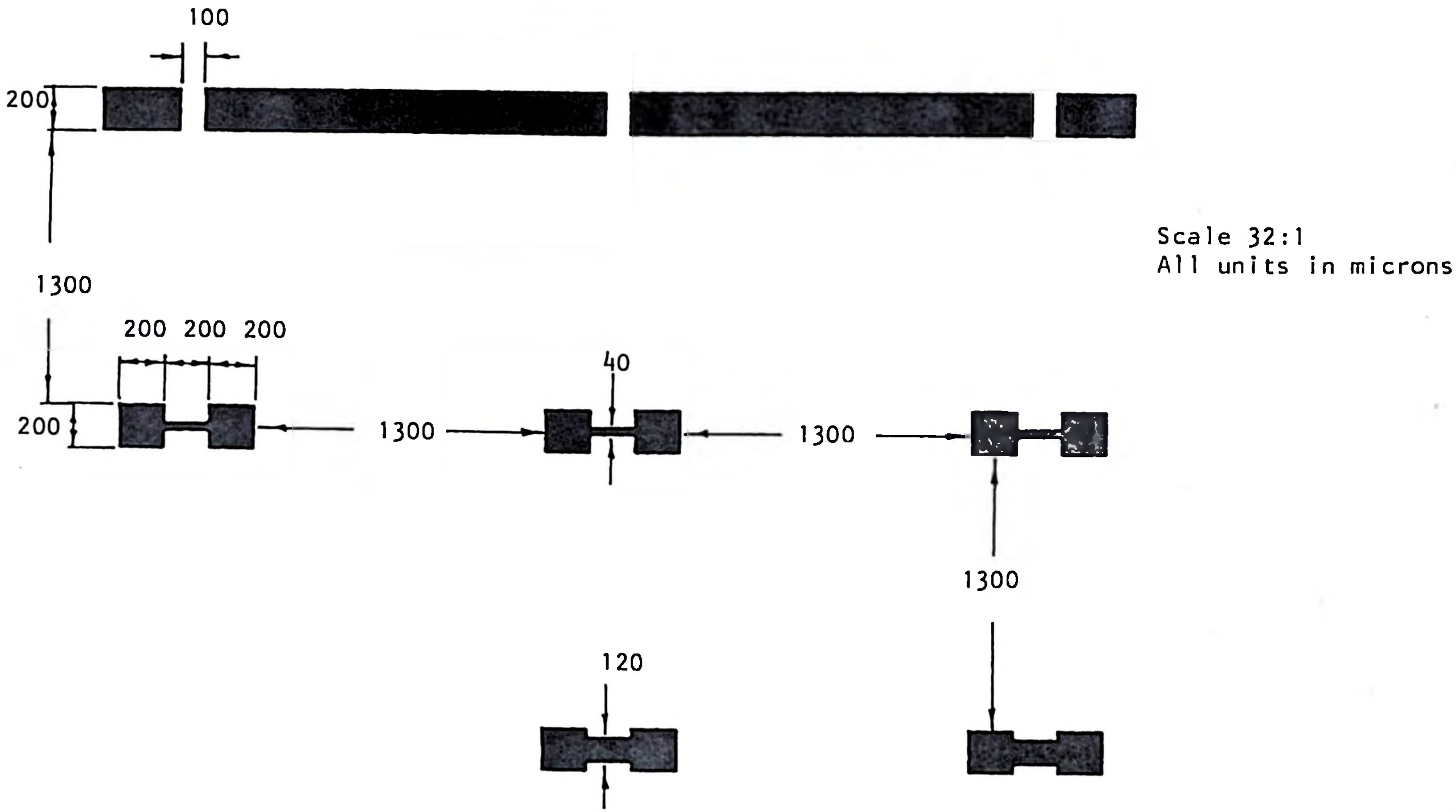

Figure 3.5 Enlarged view of mask set level 1 (a)

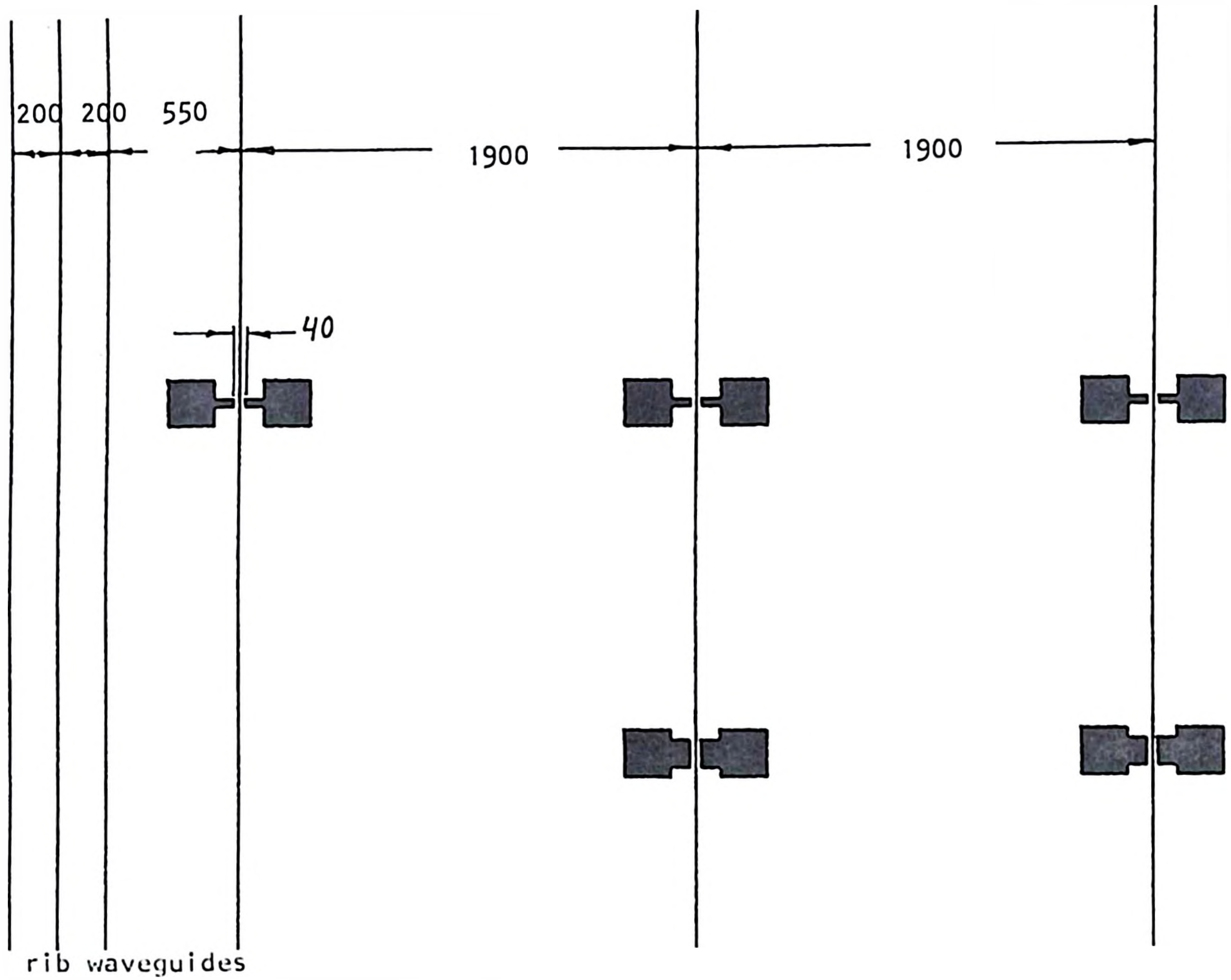

Scale 32:1
All units in microns

Figure 3.5 Enlarged view of mask set level 2 and 3 (b).

detector has a coupling length of 120 μm and should absorb nearly all the remaining optical power (44 percent). The trailing detector was intentionally not made completely absorbing (i.e. the coupling length arbitrarily long) as it was anticipated that some light would be needed for verifying ideal alignment of the waveguide with the optical source: this was the case for the IR measurements.

The device fabrication by conventional photolithographic methods is identical to the couplers. The step–by–step sequence (Fig. 3.6) is as follows. Using mask 1, tapered windows in the SiO_2 are etched for the IWDC detector pad and coupling region (step 1; Fig. 3.6) and the SiO_2 is regrown to the desired thickness (0.4 μm) (step 2). Mask 2 is then used to re–open the detector pads to bare silicon (step 3) followed by e–beam evaporation of gold. The same mask is then used to etched the excess gold with potassium iodide (step 5). Glass was sputtered over the wafer followed by defining and etching the rib waveguides using mask 3 (steps 6–7). The detectors were made ohmic by annealing the wafer at 400 ^{o}C for 10 minutes since gold on n–silicon normally forms Schottky contacts. Electrical contact to the detectors was made by ultrasonically bonding gold wires, then the sample was mounted in a jig for testing. The devices were fabricated on 2 inch (100) n–silicon substrates with 1–4 Ω–cm resistivity. Optical microscope photographs of a fabricated 2X2 switch and of a single IWDC is shown in Fig. 3.7 and Fig. 3.8, respectively.

The individual detectors' I–V characteristics were measured and the approximate "full–bias" point, which we define as the voltage which dissipates $\approx$100 W/cm^2 in the device is determined – the so–called thermal transfer region. Although, the responsivity was measured beyond this voltage, larger voltages than

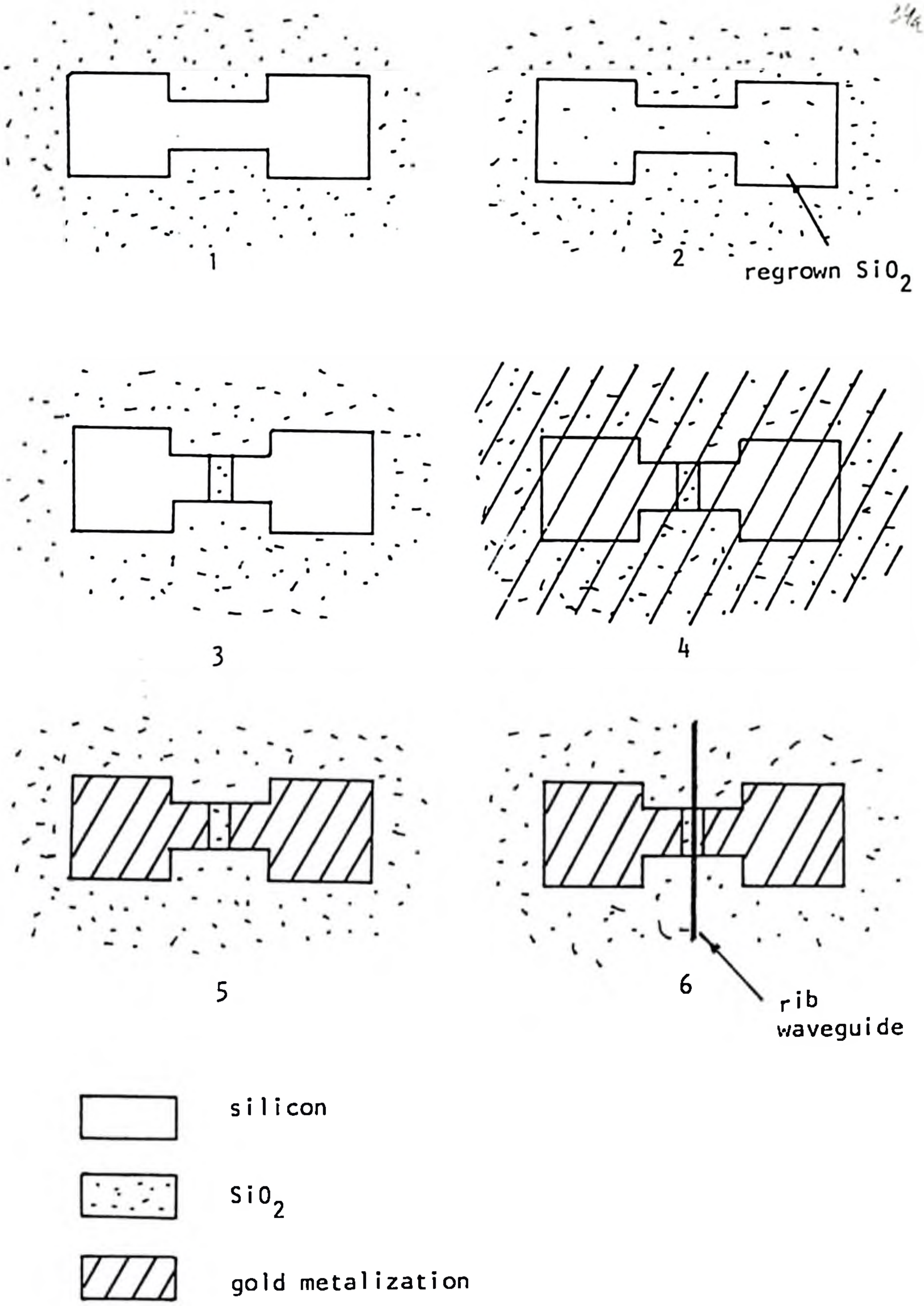

Figure 3.6 Fabrication sequence for IWDCs.

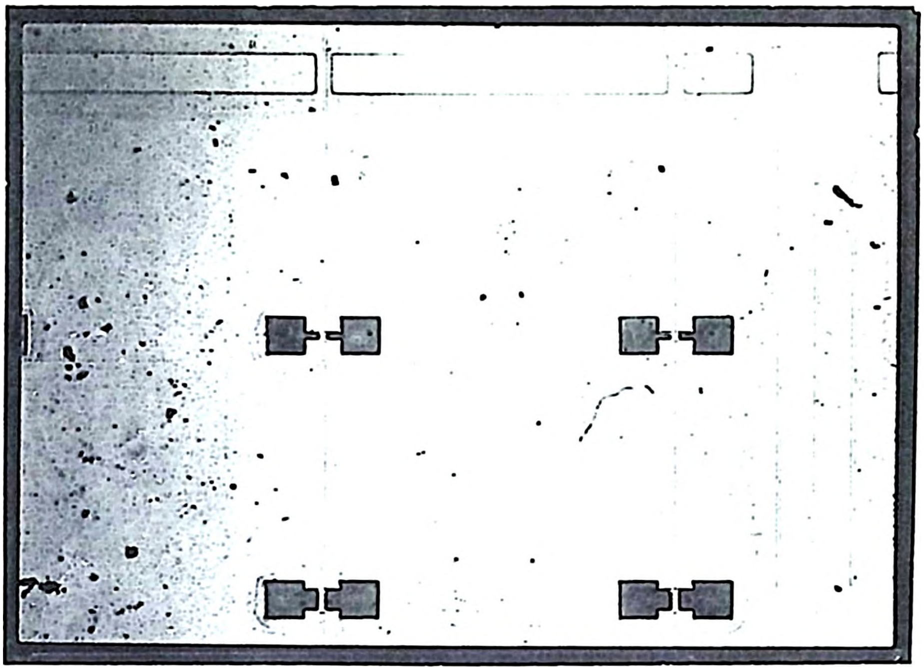

Figure 3.7 Top view of a fabricated 2X2 switch.

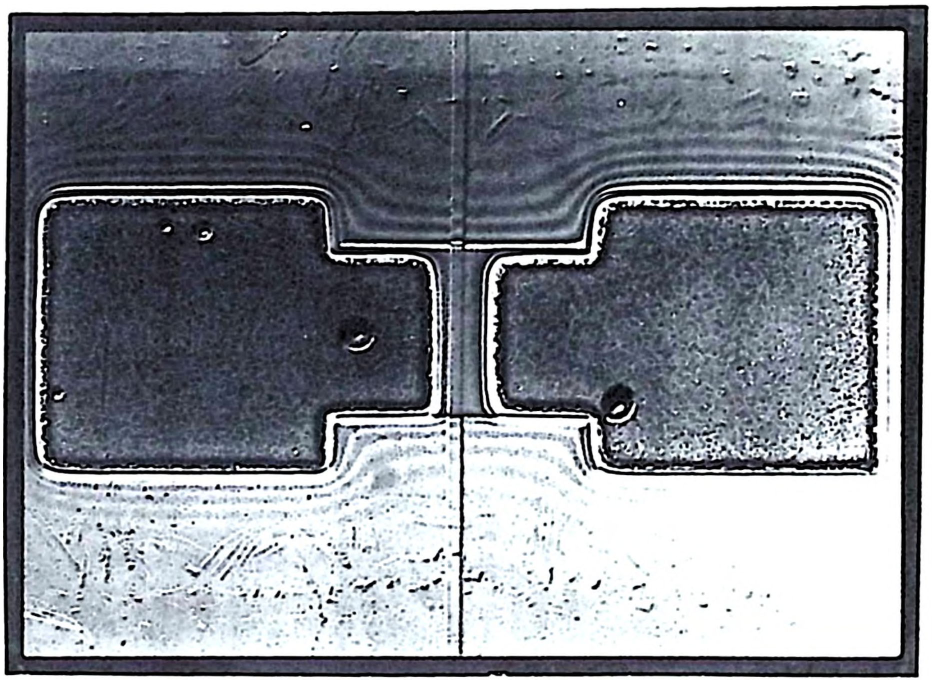

Figure 3.8 Top view of a single IWDC.

this was not used in the power splitter measurements because of some noticeable thermal lag in the response. The λ=0.6328 μm and λ=0.845 μm responsivity versus bias voltage is measured by surface illumination with a chopped HeNe laser or GaAs diode laser, focused onto the detector by a 20X microscope objective. The focused spot is positioned over the waveguide in the detector gap by monitoring the retro–reflection via a pellicle beamsplitter and imaged with an eyepiece or an IR vidicon. The observed HeNe spot size is $\lesssim$ 5 μm and the GaAs laser is asymmetric and about $\lesssim$ 5 μm by 20 μm. For the GaAs laser, the long dimension of the spot is aligned parallel to the waveguide for these and subsequent measurements. The chopping frequency was 1 kHz and the signal was detected by synchronous detection with a lock–in amplifier. The input light incident onto the objective and the reflected light from the detector surface was measured and correcting for the transmission of the objective (77 percent) the responsivity of the detector was determined. To avoid error when measuring the reflected light from the sample the photodetector is apertured to separate this light from the reflected light from the first surface of the objective.

Some detectors showed a moderate to strong photoresponse non–uniformity across the 40 μm gap of the detector, with the highest response near the negative electrode; see the next section. To mitigate the error caused by a lateral displacement of the waveguide toward one of the electrodes some samples were measured with both voltage polarities. An example of a non–uniform response is plotted in Fig. 3.9.

The optical power splitting ratio between the "lead" and "trailing" IWDC (see Fig. 3.4) can be determined by coupling into the waveguide as in section

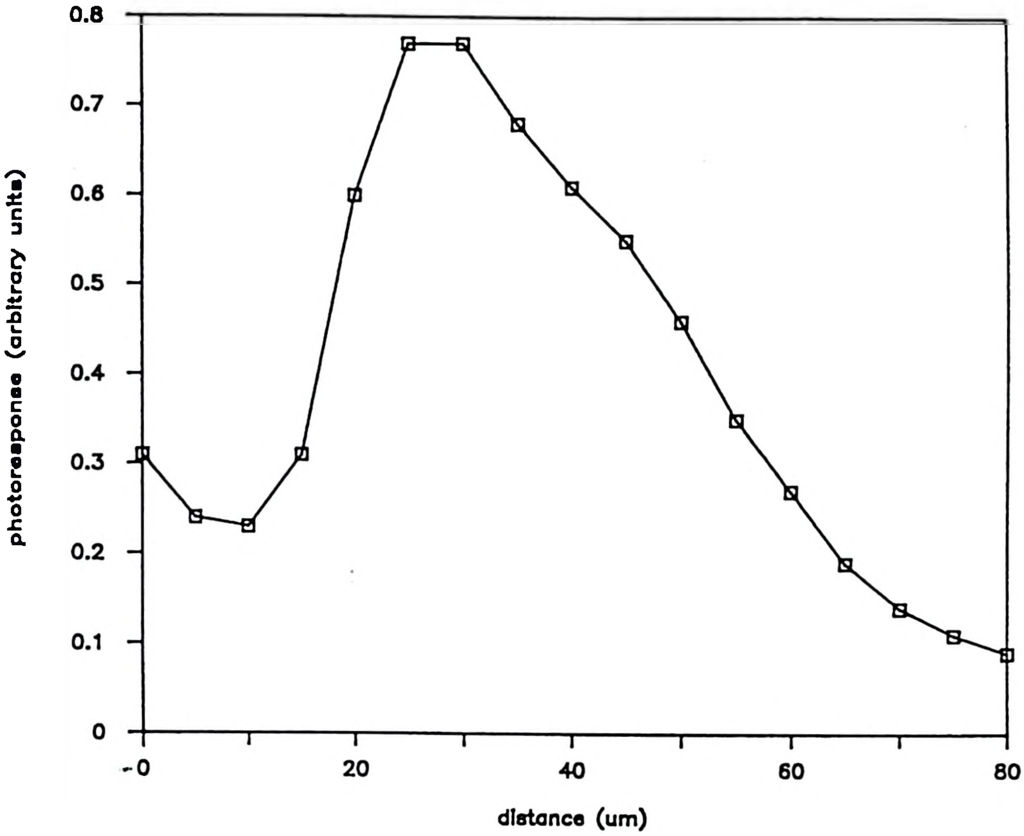

Figure 3.9 Example of a non–uniform photoresponse across the 40 μm gap of a silicon photoconductive detector.

2.5, measuring the ratio of photocurrent and correcting for differential responsivity. The ratios were measured versus bias and averaged. For λ=0.6328 μm, the HeNe laser was mechanically chopped at 1 kHz, and as will be shown in the next section the crosstalk contribution to the splitter ratio is negligible (better than –35 dB). At λ=0.845 μm an RCA C86000E diode laser was modulated at 50 kHz. In both cases the signal was detected by conventional lock–in methods.

Preliminary experiments showed that the photocurrent in one detector was dependent on the DC bias of the other because of the electrical interconnection between all pads through the substrate. Accurate measurements can be made only by independently biasing and measuring a detector while disconnecting the other.

The diffusion current crosstalk between adjacent detectors (e.g. between 1 and 2 in Fig. 3.3) is measured with the HeNe laser at chopping frequencies from 500 Hz to 2 kHz, by both surface and in–waveguide illumination. The important measurement is the crosstalk measured using a Hewlett–Packard 8557A spectrum analyzer and a high speed modulated GaAs laser. A modulated 820 nm Laser Diode Labs LCW–10 GaAs laser with a typical time–averaged output of 1 mW was focused on the detector surface by a 20X microscope objective. The crosstalk, defined as the measured signal for the beam displaced away from the detector compared to the signal on the detector was determined from 2–340 MHz and offset distances up to 200 μm.

The on/off (biased/unbiased) isolation of the detector was measured using the spectrum analyzer versus bias voltage of 6V and/or 12 V and modulation frequency from 2 to 340 MHz. For all measurements, the non–linear laser L–I was exploited to measure the second harmonic modulation signal which had a wider dynamic range because of lower RF noise: all frequencies are quoted as the second harmonic. The experimental set–up and alignment procedures are as above for the responsivity measurements.

Finally, the impulse time response of the detector was measured with a 820 nm laser with 70 ps (FWHM) pulses (Optoelectronics LCU10) and a Tektronix 7904/7S11/7T11 sampling scope with an Optoelectronics SE10 signal enhancer. The detectors were mounted on fast micro–strip test boards (although the detectors were slow enough that this wasn't necessary) and alignment of the laser to the detector is as for the responsivity measurements.

3.4 Results

Two wafers (samples 125 and 126) were processed for the 2x2 switch demonstration. The fabricated lead detector coupling length was 52 μm and 61 μm and the glass thickness was 0.61 μm and 0.65 μm for sample 125 and 126, respectively. The SiO_2 thickness in the coupling region (d) was 0.4 μm. For these dimensions our calculations predict a lead coupler value of 2.4 dB and 2.5 dB for the TE polarization, for sample 125 and 126 respectively. The length of the trailing detector was 130–140 μm for both samples.

Two complete 2x2 switches on sample 125 and half of one on sample 126 were tested. The dark resistance, responsivity at full bias, 6 and 12 V (for λ=0.6328 μm and λ=0.845 μm) and power splitting of each optical input arm are tabulated in Table 3. The dark resistance of detectors on sample 126 is typically

Table 3 Summary of the 2x2 switch measurements (IWDC detector performance and power splitting). Data grouped as a device is for the lead and trailing detector of a single optical input channel.

device	dark resistance lead/trail (ohms)	0.6328 um responsivity (A/W) lead/trail: voltage (V) full bias	6 V	12 V	0.845 um responsivity (A/W) lead/trail: voltage (V) full bias	6 V	12 V
125/1	96/66	0.36/0.35:2 V	0.79/0.83	-	0.42/0.38:2 V	1.04/0.99	-
125/2	74/87	0.38/0.31:2.5 V	0.87/0.73	-	0.47/0.52:2.5 V	0.97/1.0	-
125/3	92/71	0.16/0.41:2.5 V	0.51/0.83	-	0.27/0.47:2.5 V	0.57/1.0	-
125/4	95/79	0.41/0.29:2.5 V	0.69/0.57	-	-	-	-
126/1	433/462	0.32/0.32:6 V	same	1.24/1.17	0.38/0.56:6 V	same	1.07/1.36

device	0.6328 um TE lead/trail power splitting ratio	0.845 um TE lead/trail power splitting ratio	0.6328 um TE detector coupling efficiency *
125/1	1.06$\pm$.02	4.1$\pm$0.1	0.7$\pm$0.3
125/2	1.00$\pm$.01	2.7$\pm$0.5	0.8$\pm$0.4
125/3	0.92$\pm$.06	1.5$\pm$0.3	0.16$\pm$.05
125/4	1.6$\pm$.3	-	0.4$\pm$0.2
126/1	0.86$\pm$.05	-	1.4$\pm$.4

* 1 is 100 percent coupling efficiency

450 Ω and much higher than on 125; typically 90 Ω. The low resistance for sample 125 (large dark current) limits the "full bias" responsivity to maximum values of 0.3–0.5 A/W which is $\lesssim$ unity gain for this wavelength. A typical dark current versus bias of a detector from each wafer is shown in Fig. 3.10, which are reasonable ohmic characteristics. Only a few measurements were made on sample 126 because most of the detector contacts were open–circuited. This is probably due to incomplete opening of the SiO_2 in the detector pads and is a unique occurence as numerous detectors of this type have been fabricated.

As mentioned previously, some detectors had a non–uniform photoresponse across the detector gap (i.e. transverse to the waveguide). This is probably due to imperfect ohmic contacts with a strong edge response from a depletion region at the negative contact (more below).

On sample 125 and 126, the power splitting (lead/trailing detected power ratio) at λ=0.6328 μm measured by coupling into one input channel of the 2X2 switch and measuring the photoresponse of the detectors, was near the design value of unity. This confirms the correctness of the leaky wave calculations and the control of the coupling in the IWDC structures.

Also tabulated in Table 3 is the coupling efficiency of the couplers, which is the ratio of the detected signal to expected detected signal. The expected detected signal is determined from the measured coupling efficiency and waveguide loss (section 2.6). The accuracy of these results are limited to 30–50 percent because of the variance of the waveguide loss due to random processing variables, but the data indicates that this efficiency may be near unity. Previous work on

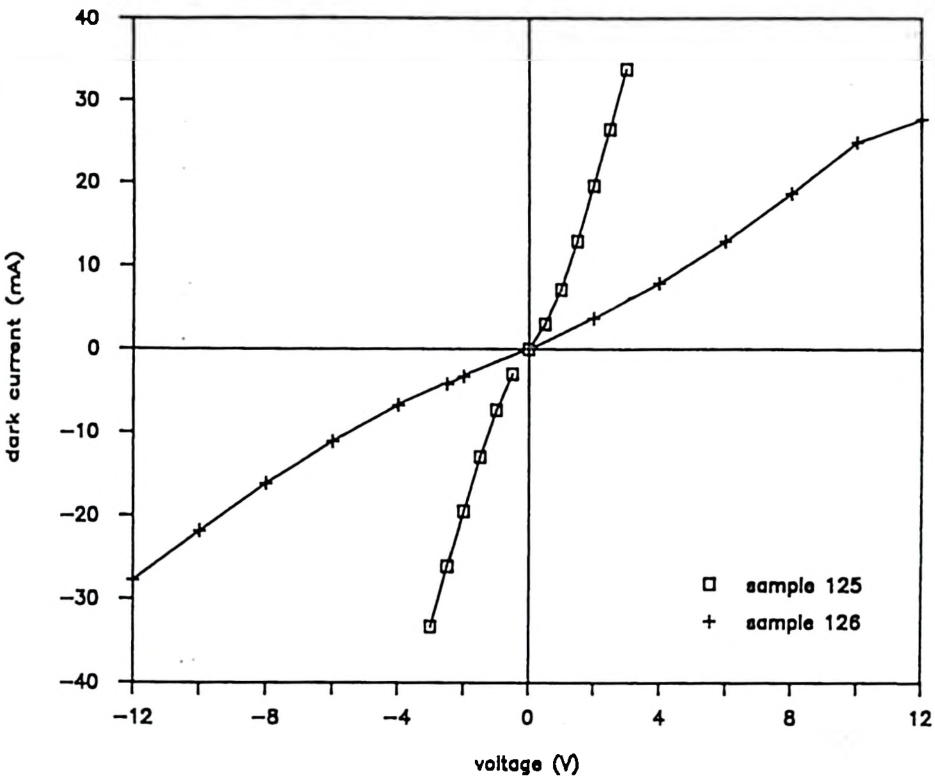

Figure 3.10 Typical dark I–V characteristics of silicon photoconductive detectors.

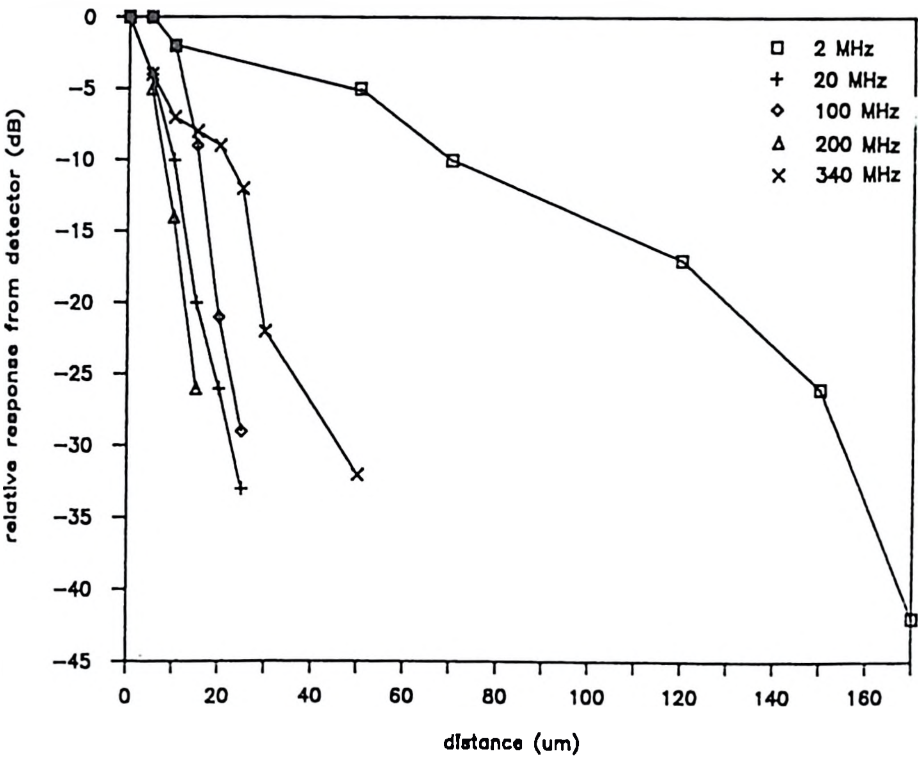

Figure 3.11 Typical diffusion current crosstalk versus offset distance and frequency.

integrated waveguide–detectors at McMaster has also seen high coupling efficiencies [52].

The crosstalk between adjacent detectors (in different optical input arms of the 2X2 switch) was measured by both surface and in–waveguide illumination of one detector while monitoring the photoresponse on the other using the HeNe laser chopped from 500 Hz to 2 KHz. The average value measured for three detector pairs was –35 dB. The in–waveguide results are identical to the surface illumination results, thus the effects of slab guided light in the power splitter measurements is negligible and of no greater effect than scattered light from surface illumination.

The diffusion current crosstalk versus frequency and offset position from the detector was measured on six detectors using the modulated 820 nm GaAs laser focused on the detector surface; a typical set of results is plotted in Fig. 3.11. In binary digital transmission, the minimum signal–to–noise ratio for a bit error rate of 10^{-10} is 16 dB [53]. At modulation frequencies of 20–340 MHz, a –20 dB crosstalk figure yields an allowed detector spacing of $\lesssim$ 25 μm or a crosspoint density of $\gtrsim$ 160 000 cm^{-2}.

The typical on/off (biased/unbiased) detector isolation from 2–340 MHz measured with the modulated GaAs laser focused on the detector surface and the photosignal fed to a spectrum analyzer, is plotted in Fig. 3.12. The best value of ≈ 35 dB at 12 V bias on the larger resistivity sample 126 is not good compared to the 70 dB value measured by MacDonald et al. for GaAs photoconductors [47]. It is also extremely unusual that for sample 125 the isolation decreased with increasing frequency; no explanation can be offered. MacDonald et al. have also concluded

79a

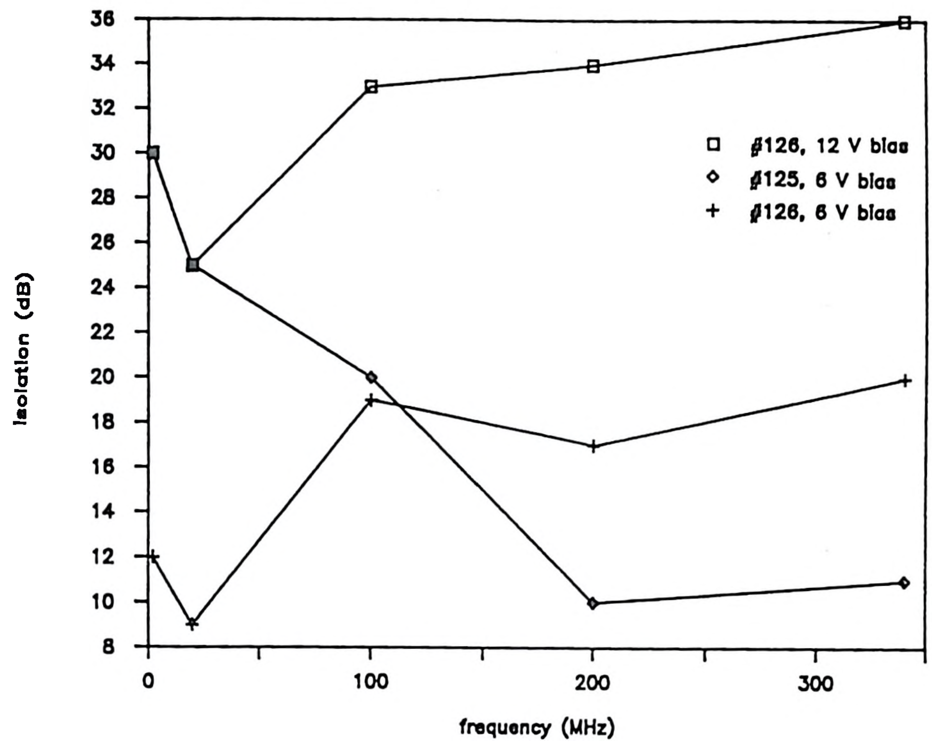

Figure 3.12 Typical detector isolation versus frequency and bias.

that degraded isolation and non–uniform response in the detector gap is probably due to imperfect ohmic (Schottky–like) contacts which has an unbiased photovoltaic response.

A typical impulse time response measured with the 70 ps GaAs laser focused on the detector, for a detector from sample 126 at a bias of 12 V and 6 V is shown on comparable scales in Fig. 3.13(a)–(b). The rise time is 15 ns with a FWHM impulse time response of 120 ns. This is much slower than desired for moderate bit–rate (100–500 MHz) switching systems, in fact it seems surprisingly large. At 12 V, the field across the detector gap is 3×10^{3} V/cm and using the "low field" mobility for the slow hole carriers of 480 cm^2/V–s (for low doping, $\leq 10^{16}$ cm^{-3}) yields a carrier transit time of 3 ns for our device. This figure is comparable to detectors previously fabricated for integrated optics experiments at McMaster with a detector gap of 15–20 μm on 10 Ω–cm p–silicon which had an impulse time response of "a few ns" [52]. If our detectors are non–ohmic the electric field is probably much smaller than calculated above as a large fraction of the applied potential is dropped across the depletion region. Shown in Fig. 3.13(c) is the impulse time response with the spot illumination near the negative electrode. Note the faster (≈25 ns) fast part of the response which is indicative of illuminating the depletion region of a non–ohmic contact.

The use of these detectors for high speed applications need to be re–examined, but they have been sufficient to demonstrate the feasability of a monolithically integrated and compact optoelectronic switch.

Measurements of the splitter ratio for the 845 nm laser and TE modes were also taken (Table 3). Of three pairs of detectors the average lead/trailing

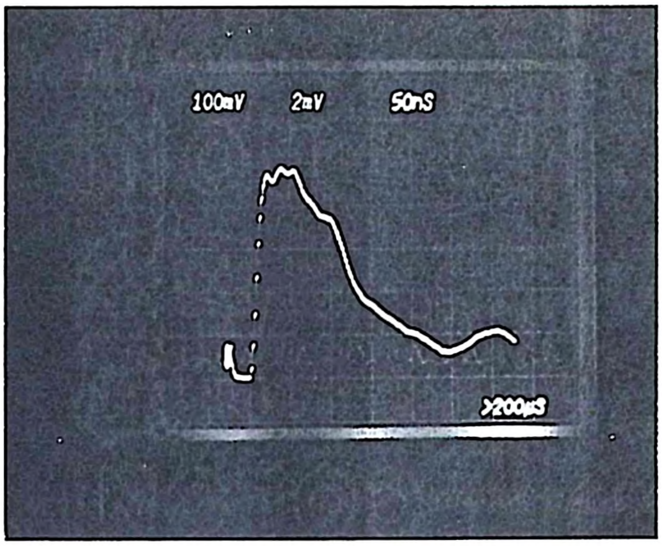

(a)

50ns

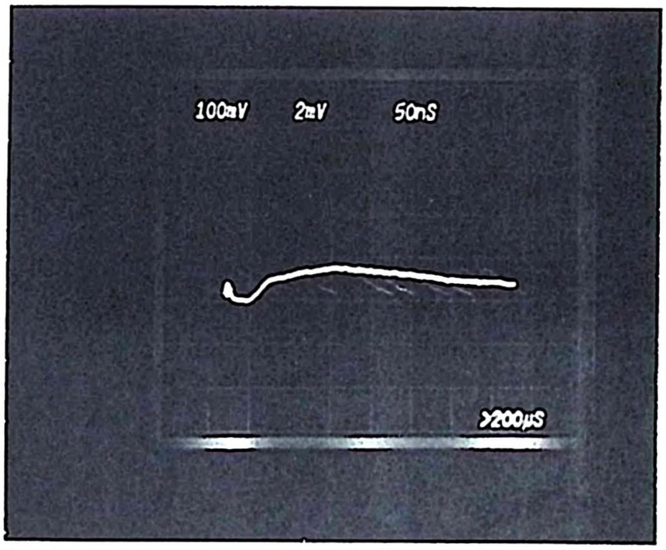

(b)

Figure 3.13 Detector response at 12 V bias (a), 6 V bias (b).

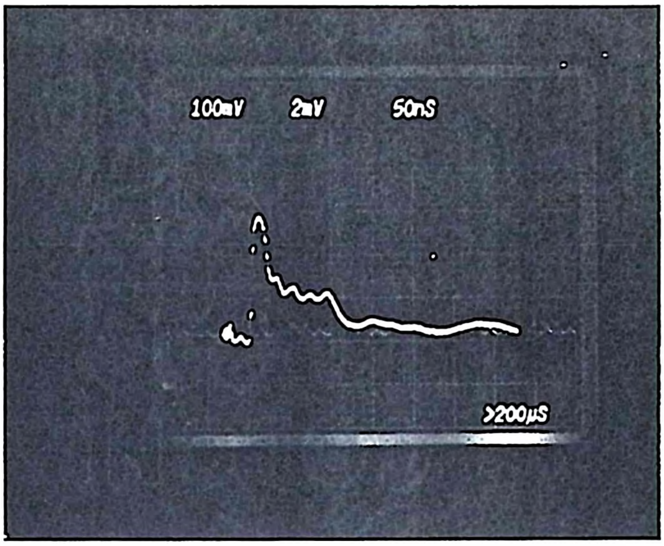

50 ns

(c)

Figure 3.13 Detector response at 12 V bias with the spot illumination near the negative detector pad (c).

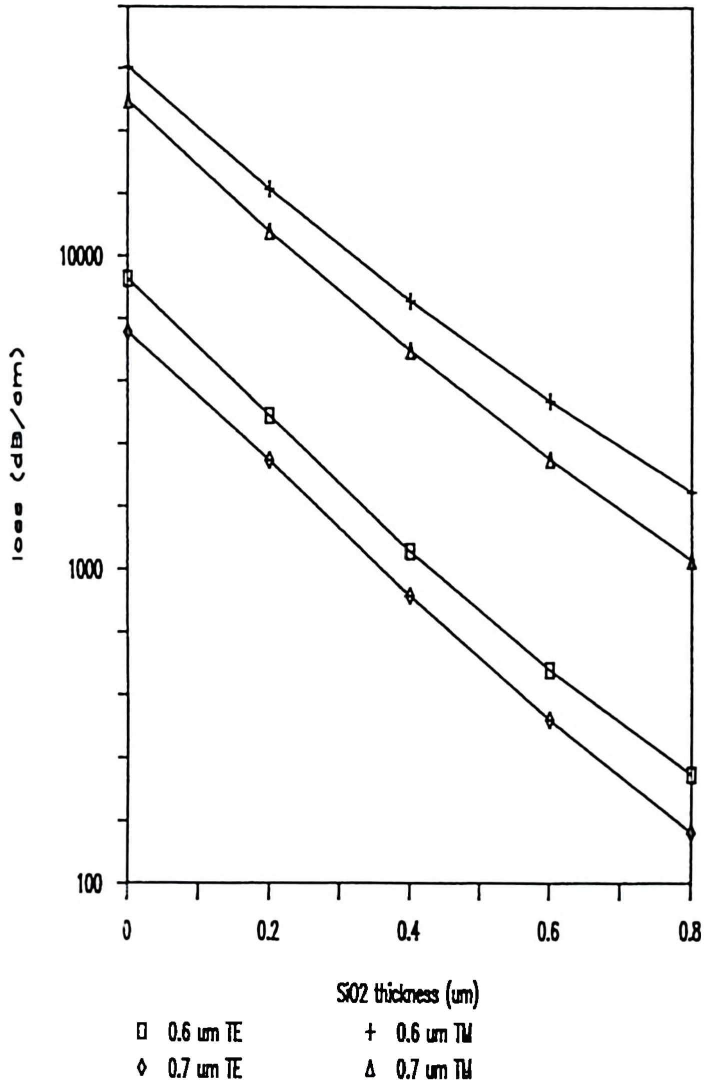

Figure 3.14 Theoretical leaky wave loss for a=0.6 μm and 0.7 μm for TE_0 and TM_0 modes at λ=0.845 μm.

detector power splitting ratio was determined to be 3.7±0.2 (i.e. 79 percent of the incident power is absorbed in the lead detector), which corresponds to a lead coupler of 6.7±0.2 dB. At λ=0.6328 μm the lead coupler is 3 dB so the λ=0.845 μm result is 2.2 times larger. For comparison, the TE theoretical leaky wave loss at λ=0.845 μm is plotted in Fig. 3.14, using the known dispersion of the refractive index for SiO_2 which is ≈0.004 smaller at 0.845 μm compared to 0.6328 μm and the tabulated silicon complex index of $3.67-j0.005$[20]. For example, for a glass thickness of 0.6 μm and an SiO_2 thickness of 0.4 μm, the ratio of the leaky loss at 0.845 μm compared to 0.6328 μm is 2.9 which is similar to our experimental value of 2.2. Even taking into account the uncertainty in the SiO_2 refractive index, a variation in the real silicon index of 0.03 and a variation of the silicon absorption coefficient by 20 percent does not vary the theoretically calculated loss by more than 6 percent, so there is still not complete agreement with theory for the IR power splitting. In addition the wavelength of the laser published by the manufacturer was verified by measurement with a calibrated monochromator and was accurate to ±2 nm (variance from the different longitudinal laser modes).

CHAPTER 4

CONCLUSIONS

The leaky wave losses of an integrated waveguide–detector coupler structure in the Corning 7059 glass/SiO_2/silicon system at a wavelength of 0.6328 μm has been theoretically modelled and experimentally measured. The theoretical analysis of the four–layer leaky waveguide structure by exact numerical and approximate methods has been compared, and the first–order perturbation solutions are found to be good for waveguides well above cut–off: these solutions are considerably faster to obtain than the exact solutions. The leaky waveguide losses are strongly dependent on mode order, waveguide structure – particularly the SiO_2 thickness – and polarization; the latter being unique to the silicon/glass system because of the large index ratio between the waveguide and the substrate.

The taper structure in the IWDC has been approximately analyzed and found that the tapers should be much longer than 15 μm and be smooth gradual transitions to minimize radiation losses in the tapers, mode conversion amongst the leaky modes and depolarization (polarized mode conversion).

Numerous couplers with SiO_2 thicknesses from 0.15 μm to 0.8 μm were fabricated and the leaky losses measured for both TE and TM polarization. The results were in good agreement with theory. The samples suffered from uniformity problems in the waveguides which contributed to variable loss within each device, but a large number of measurements reduced the errors. The measurements would have been easier if the processing of the waveguides and the fabrication of the tapers were more consistent, in fact at present the taper length and shape is difficult to control because of the photoresist undercutting required to fabricate them. Waveguide scatter loss is not uniform amongst the waveguides. It has been noted that waveguide depolarization can be an important effect in IWDCs fabricated in this system because of the large anisotropic polarization–dependent loss.

The first monolithically integrated 2X2 optoelectronic switch has been demonstrated with four IWDCs as switching crosspoints. The passive power splitting (at λ=0.6328 μm) is close to the ideal value of fifty percent but the photoconductive silicon detectors are not optimum. The fabricated silicon photoconductive detectors had a low dark resistance (90 Ω on sample 125), a best isolation of 35 dB and an impulse time response of 120 ns (at 12 V bias). The gold on (100) n–silicon showed non–ohmic characteristics which degraded the isolation, speed and photoresponse uniformity across the detector surface. The latter is important since in our structures the waveguides (of width 9 μm) is smaller than the detector gap width of 40 μm. After repeated annealing the detectors could not be improved. It is possible that the problems can be eliminated if (100) 10 Ω p–silicon is used because good photoconductive silicon detectors have been demonstrated in the past on the same material but with (111) orientation [52]. A more interesting and technologically important alternative is to fabricate the device on a GaAs substrate: this should be viable since CVD SiO_2 has recently been implemented and GaAs photoconductors have been fabricated in the past at McMaster. In addition, the GaAs photoconductors should be faster (except at saturated carrier velocities) due to the high ("low field") electron mobility and short carrier lifetime (few ns).

For photogenerated carrier diffusion limited crosstalk at 20–340 MHz of –20 dB, detector crosspoint densities of >160 000 cm^{-2} are possible. The limit on the switch density will probably be restricted by electrical crosstalk, metalization connection routing to all elements and the taper length. For example, our taper lengths are typically 50 μm and with a coupling length of 40 μm and a detector gap size of 40 μm, the upper limit on the crosspoint density is 18 000 cm^{-2}. At this density a 100x100 switch would be less than one square This is much more compact than the 72 cm long $LiNbO_3$ directional coupler (all–optical) switch discussed in section 3.2. In addition, optical fiber interconnects to the IWDC optoelectronic switch is reduced by N^2–N (for an NxN switch) compared to the previously demonstrated discrete component switch [48].

REFERENCES

1. S.E. Miller, "Integrated optics – an introduction", Bell Syst. Tech. J. 48, 2059 (1969).

2. C.W. Pitt, F.R. Geller and R.J. Stevens, "R.F. Sputtered Thin Films for Integrated Optical Components", Thin Solid Films 26, 25 (1975).

3. H. Inoue, K. Hiruma, K. Ishida, H. Sato and H. Matsumura, "Switching characteristics of GaAs directional coupler optical switches", Appl. Opt. 25, 1484 (1986).

4. A. Yariv and M. Nakamura, "Periodic structures for integrated optics", IEEE J. Quantum Electron. QE–13, 233 (1977).

5. T.H. Wood, C.A. Burrus, R.S. Tucker, J.S. Weiner, D.A.B. Miller, D.S. Chemla, T.C. Damen, A.C. Gossard, W. Wiegmann, "100 ps waveguide multiple quantum well optical modulator with 10:1 on/off ratio", Electron. Lett. 21, 693 (1985).

6. U. Koren, T.L. Koch, H. Presting and B.I. Miller, "InGaAs/InP multiple quantum well waveguide phase modulator", Appl. Phys. Lett. 50, 368 (1987).

7. F.K. Reinhart, J.C. Shelton, R.A. Logan and B.W. Lee, "MOS rib waveguide polarizers", Appl. Phys. Lett. 36, 237 (1980).

8. H. Nakano, S. Yamashita, T. Tanaka, M. Hirao and M. Maeda, "Monolithic Integration of Laser Diodes, Photomonitors and Laser Driving and Monitoring Circuits on a Semi–Insulating GaAs", J. Lightwave Tech. LT–4, 574 (1986).

9. P. Granestrand, B. Stolz, L. Thylen, K. Bergvall, W. Doldissen, H. Heinrich and D. Hoffmann, "Strictly nonblocking 8x8 integrated optical switch matrix", Electron. Lett. 22, 816 (1986).

10. M. Erman, P. Jarry, R. Gamonal, J. Gentner, P. Stephan and C. Guedan, "Monolithic Integration of a GaInAs p–i–n Photodiode and an Optical Waveguide: Modeling and Realization using Chloride Vapor Phase Epitaxy", J. Lightwave Tech. 6, 399 (1988).

11. W.C. Borland, D.E. Zelmon, C.J. Radens, J.T. Boyd and H.E. Jackson, "Properties of Four–Layer Planar Optical Waveguides Near Cutoff", IEEE J. Quantum Electron. QE–13, 1172 (1987).

12. S. Dutta, H.E. Jackson and J.T. Boyd, "Extremely low–loss glass thin film optical waveguides utilizing surface coating and laser annealing", J. Appl. Phys. 52, 3873 (1981).

13. J.T. Boyd and C.C. Chen, "Integrated optical silicon photodiode array", Appl. Opt. 15, 1389 (1976).

14. J.T. Boyd and C.C. Chen, "An integrated optical waveguide and charge–coupled device image array", IEEE J. Quantum Electron. QE–13, 282 (1977).

15. K.A. James, R.R. August and J.E. Coker, "Silicon, monolithic optical integrated circuits for laser system applications", Radio Science 12, 529 (1977).

16. D.B. Ostrowsky, R. Poirer, L.M. Reiber and C. Deverdun, "Integrated Optical Photodetector", Appl. Phys. Lett. 22 , 463 (1973).

17. K. Tsutsumi, Y. Imada, H. Hirai and Y. Yuba, "Analysis of Single–Mode Optical Y–junctions by the Bound Step and Bend Approximation", J. Lightwave Tech. 6, 590 (1988).

18. W. J. Minford, S.K. Korotky and R.C. Alferness, "Low–loss Ti:$LiNbO_3$ Waveguide Bends at λ=1.3 μm", IEEE Trans. Microwave Theory and Tech. MTT–30, 1790 (1982).

19. E.A. Taft, "Index of Refraction of Steam Grown Oxides on Silicon", J. Electrochem. Soc. Solid State 125, 993 (1970).

20. E.D. Palik, Handbook of Optical Constants of Solids, Academic, Orlando (1985), pp.565,760.

21. A. Yariv, Quantum Electronics, 2nd Ed., Wiley, New York (1975), pp. 539–541.

22. G. Mak, M. Eng. Off–Campus Project, McMaster University, Hamilton, Ontario (1988).

23. W. Streifer, R.D. Burnham and D.R. Scifres, "Substrate Radiation Losses in GaAs Heterostructure Lasers", IEEE J. Quantum Electron. QE–12, 177 (1976).

24. D.B. Hall and C. Yeh, "Leaky waves in a heteroepitaxial film", J. Appl. Phys. 44, 2271 (1973).

25. L.M. Walpita, "Solutions for planar optical waveguide equations by selecting zero elements in a characteristic matrix", J. Opt. Soc. Am. A 2, 595 (1985).

26. M.J. Adams, An Introduction to Optical Waveguides, Wiley, Chichester (1981), pp. 28–31, 75–82.

27. H. Kolgenik and V. Ramaswamy, "Scaling Rules for Thin–film Optical Waveguides", Appl. Opt. 13, 1857 (1974).

28. E.A.J. Marcatili and S.E. Miller, "Improved Relations Describing Directional Control in Electromagnetic Waveguidance", Bell Syst. Tech. J. 48, 2161 (1969).

29. D. Marcuse, Light Transmission Optics, 2nd Ed., Van Nostrand, Princeton (1982).

30. Y. Takuma, M. Miyagi and S. Kawakami, "Bent asymmetric dielectric slab waveguides: a detailed analysis", Appl. Opt. 20, 2291 (1981).

31. R.G. Hunsperger, A. Yariv and A. Lee, "Parallel end–butt coupling for optical integrated circuits", Appl. Opt. 16, 1026 (1977).

32. D. Marcuse, "Tilt, Offset and End–Separation Loss of Lowest Order Slab Waveguide Mode", J. Lightwave Tech. LT–4, 1647 (1986).

33. A.W. Snyder and J.D. Love, Optical Waveguide Theory, Chapman and Hall, London (1983), pp.483–485, 499–500.

34. J.E. Bowers and C.A. Burrus, "Ultrawide–Band Long–Wavelength p–i–n Photodetectors", J. Lightwave Tech. LT–5, 1339 (1987).

35. P.E. Gise and R. Blanchard, Semiconductor Integrated Circuit Fabrication Techniques, Fairchild Corp. (1979).

36. R. Weir, M.Eng. Thesis, McMaster University (1987).

37. H. Jerominek, S. Patela, J.Y.D. Pomerleau, C. Delisle and R. Tremblay, "Some Properties of R.F. Planar Magnetron–Sputtered Corning 7059 Glass Films", Thin Solid Films 146, 191 (1987).

38. W. Stutius and W. Streifer, "Silicon nitride films on silicon for optical waveguides", Appl. Opt. 16, 3218 (1977).

39. E.M. Garmire and K. Honda, "Depolarization in Channel Glass Waveguides", J. Lightwave Tech. LT–4, 220 (1986).

40. P.G. Suchoski, T.K. Findakly and F.J. Leonberger, "Depolarization in Ti:$LiNbO_3$ waveguides and its effect on circuit design", Electron. Lett. 23, 1357 (1987).

41. D. Marcuse, "Mode Conversion Caused by Surface Imperfections of a Dielectric Slab Waveguide", Bell Syst. Tech. J. 48, 3188 (1969).

42. G.I. Parisi, S.E. Haszko, G.A. Razganyi, "Tapered Windows in SiO_2: The Effect of NH_4:HF Dilution and Etching Temperature", J. Electrochem. Soc. Solid State 124, 917 (1977).

43. R.I. MacDonald and E.M. Hara, "Optoelectronic broadband switching array", Electron. Lett. 14, 502 (1978).

44. K. Aida, K. Matsuno and M. Toyoshima, "Design and Performance of an Optoelectronic Matrix Switch Using Si–p–i–n Photodiodes", J. Lightwave Tech. 6, 131 (1988).

45. D.J. Blumenthal, P.R. Prucnal, L. Thylen and P. Granestrand, "Performance of an 8x8 $LiNbO_3$ switch matrix as a gigahertz self–routing switching node", Electron. Lett. 23, 1359 (1987).

46. D.K.W. Lam and R.I. MacDonald, "Fast Optoelectronic Crosspoint Electrical Switching of GaAs Photoconductors", IEEE Electron Device Lett. EDL–5, 1 (1984).

47. R.I. MacDonald, D.K.W. Lam, R.H. Hum and J.P. Noad, "Monolithic Array of Optoelectronic Broadband Switches", IEEE J. Solid State Circuits SC–19, 219 (1984).

48. R.I. MacDonald and D.K.W. Lam, "Optoelectronic Switching Matrices: recent developments", Opt. Eng. 24, 220 (1985).

49. H.J. Klein, R. Kaumanns and H. Beneking, "High–Speed $Ga_{0.47}In_{0.53}As$ photoconductive detector for picosecond light pulses", Electron. Lett. 17, 421 (1981).

50. M.J. Robertson, S. Ritchie and P. Dayan, "Semiconductor waveguides: Analysis of coupling between rib waveguides and optical fibres", Soc. Photo. Instrum. Eng. 578, 184 (1985).

51. H. Inoue, K. Hiruma, K. Ishida, T. Asai and H. Matsumura, "Low Loss GaAs Optical Waveguides", IEEE Trans. Electron. Dev. ED–32, 2662 (1985).

52. P.E. Jessop, B.K. Garside and D.M. Bruce, "High Speed Switching for Integrated Optical Applications: Phase II Final Report", Department of Communications Contract No. OST85–00241 (1987).

53. Members of Technical Staff of Bell Laboratories, Transmission Systems for Communications, 4th Ed., Bell Telephone Laboratories, New York (1971), pp. 703–707.

54. R.A. Spanke, "Architectures for Large Nonblocking Optical Space Switches", IEEE J. Quantum Electron. QE–22, 964 (1986).